國 立 交 通 大 學

光電工程研究所

碩 士 論 文

氖氣/氬氣混合之運用厚膜光阻形成阻隔壁之微電漿元件特性之研究

Characterization of Micro-plasma Devices Using Thick Photoresist as a Barrier Rib in Neon-Argon Gas Mixtures

研 究 生：卓龍材 Long-Cai Jhuo

指導教授：金星吾 博士 Dr. Sung-O Kim

中 華 民 國 九 十 五 年 六 月

氖氣/氬氣混合之運用厚膜光阻形成阻隔壁之微電漿元件特性之研究

Characterization of Micro-plasma Devices Using Thick Photoresist as a Barrier Rib in Neon-Argon Gas Mixtures

研 究 生：卓龍材　　Student：Long-Cai Jhuo

指導教授：金星吾　　Advisor：Sung-O Kim

國 立 交 通 大 學

光電工程研究所

碩 士 論 文

A Thesis

Submitted to Department of Photonics

Institute of Electro-Optical Engineering

College of Electrical and Computer Engineering

National Chiao Tung University

in partial Fulfillment of the Requirements

for the Degree of

Master

in

Electro-Optical Engineering

June 2006

Hsinchu, Taiwan, Republic of China

中華民國九十五年六月

氖氣/氬氣混合之運用厚膜光阻形成阻隔壁之微電漿元件特性之研究

碩士研究生：卓龍材　　　　　指導教授：金星吾 博士

國立交通大學　光電工程學系光電工程研究所

中文摘要

微電漿元件的研究近來提供了許多相當引人注目的特性與可能的應用。因為半導體製程技術的進步，提供微電漿元件製程的可靠度。有別於鑽孔式的方法，利用半導體製程可使元件的尺寸縮小與元件的一致性。並且可提高微電漿元件發光的穩定性與均勻性。

本篇論文闡述交錯式微電漿元件運用厚膜光阻在氬氣/氖氣混合操作下的特性研究成果。因為利用光蝕刻式玻璃當作阻隔壁，有(1)與電極對準精確性和(2)與基板有間隙的問題。所以本論文運用厚膜光阻代替光蝕刻式玻璃，因為厚膜光阻是利用旋轉塗佈的方式，所以可以解決間隙的問題。使用光罩對準曝光機可使圖形與電極對位精確。本元件放置於一真空系統提供電性產生電漿，並且量測電性與光學影像。本研究之微電漿元件可得到：穩定電壓電流特性、低操作電壓、穩定輝光放電現象。而增加氬氣濃度的參雜可有效的降低操作電壓。

Characterization of Micro-plasma Devices Using Thick Photoresist as a Barrier Rib in Neon-Argon Gas Mixtures

Student：Long-Cai Jhuo Advisor：Dr. Sung-O Kim

Department of Photonics and Institute of Electro-Optical Engineering
National Chiao Tung University

Abstract

For the past few years, microplasma devices have been investigated and pursued worldwide because of their unique electrical and optical properties. Much of the interest in microplasma devices stems from generating efficient vacuum ultraviolet (VUV) to visible radiation. Unfortunately, the exiting microplasma devices have revealed that dimensional control cannot keep consistently accurate by the drilling method. In addition, such a process for the micro-cavity fabrication is not feasible to make large sizes and hard to make stable glow discharge. Recently, the field of microelectromechanical systems (MEMS) processing technologies offers the key advantages, including small size scales, low mass, low volume, and fast response time.

The micro-plasma device using thick photoresist (SU-8) as a barrier rib has been fabricated and characterized. Operating in the abnormal mode at pressure from 300 to 800 Torr, the micro-plasma device with interdigitated electrodes has been investigated in a vacuum chamber. The discharge characteristics of pure neon, neon-1% argon and neon-5% argon gas mixtures are investigated for possible use in microplasma devices.

The electrical properties on discharge have been examined by bipolar voltage waveform with different argon gas concentration. The micro-plasma device operates at voltage as low as 190 V when neon pressure is 800 Torr. Besides, the ignition voltage of the micro-plasma device was reduced due to an increase in argon concentration.

Acknowledgement

首先要感謝指導教授金星吾老師兩年來在研究上的指導，培養我對事情有多方面的思考，並且更縝密。

在實驗室的日子裡，很高興能與吳正宇、李偉誠、任珂銳與周鴻杰同學們，在這新的實驗室裡一起努力，並且在研究過程提供許多寶貴的建議，很高興能與你們在這裡相遇，並且一起分享生活上的點點滴滴。同時也要感謝其他學長與同學在課業上、研究上、生活上的幫助與分享，陪伴我一起渡過碩士班兩年的日子。我還要感謝實驗室林義淵與楊子民學弟的努力，讓實驗室充滿歡樂的氣氛，最後還有助理張雅惠小姐的幫忙。

此外，也要感謝奈米中心彭兆光先生在機台上的幫助與訓練，讓我能順利的進行實驗。

對於我的家人與女友魏瑛君，我要感謝你們多年來的支持與鼓勵，還有在生活上的照顧與關懷，使我能夠在交通大學進行研究與學習，並且順利完成我的碩士學位。我希望這份喜悅能與各位分享。最後，也希望將這分喜悅獻給已過世的父親。

Table of Contents

Abstract (Chinese)……………………………………………………….i

Abstract (English)……………………………………………………...ii

Acknowledgement..iv

Table of Contents..v

Table Caption..vii

Figure Caption...viii

Chapter 1 Introduction……………………………………………...…1

1.1 Micro-plasma Devices…………………………………………………1

1.1.1 Cylindrical Cathode Structure………………………...…………....2

1.1.2 Pyramidal Cathode Structure..4

1.2 Applications of Micro-plasma Devices……………………………......…5

1.2.1 Micro-plasmas for biomedical and environmental applications…………6

1.2.2 Micro-plasmas for display applications……………………………..…6

1.2.3 Micro-plasmas for other Applications……………………………………7

1.3 Motivation and Objective of this Thesis…………………………........…7

1.4 Arrangement of this Thesis…………………………………………...…8

Chapter 2 Principle……………....................……………………………...…9

2.1 Introduction............……….............………..................……………….....…9

2.2 Plasma...………………………………...…9

2.3 Gas Discharges.............…………...........................…………………...…11

2.3.1 Gas Breakdown and Paschen's Law............………………...………...…11

2.3.2 Glow Discharge............………….....................…………………………...…16

2.4 Penning Effect…………………………………………………………21

Chapter 3 Fabrication and Measurement Instruments......23
3.1 Introduction......23
3.2 Semiconductor Fabrication Process......23
3.3 Measurement Instruments......31
3.3.1 Atomic Force Microscope (AFM) 31
3.3.2 Scanning Electron Microscope (SEM) 33
3.3.3 Vacuum System Setup......34
Chapter 4 Experimental Results and Discussion......41
4.1 Introduction......41
4.2 The Features of The Interdigitated Electrode Micro-Plasma Device......41
4.3 The Electrical Properties in Neon Gas......44
4.3.1 Relationship between voltage and pressure with different bipolar voltage waveform frequency......45
4.3.2 Relationship between ignition voltage and pressure with different dielectric layer thickness......48
4.4 The Electrical Properties in Neon-Argon Gas Mixtures......50
4.5 The Glow Images of the Interdigitated Electrode Micro-Plasma Device.53
Chapter 5 Conclusions......56
Reference......58

Table Caption

Table 2.1 The ionization and metastable energies of the rare gas…………………....22

Table 3.1 The RCA clean procedure…………………………………………………27

Table 3.2 The growth of 1 μm silicon oxide for Si (100)……………………………28

Table 3.3 The lithography procedure for patterning the electrode…………………...29

Table 3.4 The parameters of XP SU-8 3050 photoresist……………………………..31

Figure Caption

Fig. 1.1 General diagram of a macroscopic hollow cathode discharge device……….2

Fig. 1.2 Three Typical micro-plasma geometries……………………………….………..3

Fig. 1.3 Micro-plasma geometry with cylindrical hollow cathode and anode, separated by a mica insulator……………………………………………………………….3

Fig. 1.4 Diagram a single micro-plasma device in silicon..4

Fig. 1.5 Plane and hollow cathode configuration implemented by external wiring within the same geometry………………………………………………………..4

Fig. 1.6 Micro-plasma geometry with pyramidal cavity: (a) Cross-section diagram; (b) SEM micrograph of a single device; (c) SEM micrograph of the device cross-section, the particulate in the figure result from dicing……………………………………......5

Fig. 1.7 The photograph of micro-plasma geometry with cylindrical hollow cathode by drilling method……………………………………………………………………8

Fig. 2.1 Space and laboratory plasmas classified by their electron temperature, T_e, and charged particle density, n…………………………………………………………10

Fig. 2.2 Electron energy distribution in a weakly ionized gas, assuming a Maxwellian distribution at the average electron temperature, T_e……………………………….....11

Fig. 2.3 The diagram of the plane parallel electrode for producing a direct current (DC) glow discharge……………………………………………………………………..12

Fig. 2.4 The experimental Paschen's curves for different gases………….……….14

Fig. 2.5 Voltage-current (V-I) characteristic for a discharge…………….…………..15

Fig. 2.6 The potential distribution in a dc glow discharge process…………………..18

Fig. 2.7 The spatial distribution of (a) the luminous regions in a typical discharge and (b) the electric field……………………………………………………………..18

Fig. 3.1 The flow chart of fabrication process for micro-plasma device: (a) substrate cleaning (b) silicon oxide growth (c) metal deposition (d) dielectric layer deposition (e) barrier rib formation……………………………………………………………25

Fig. 3.2 The photograph of Wet Bench for silicon cleaning…………………………26

Fig. 3.3 The photograph of Furnace for thermal oxide………………………………27

Fig. 3.4 The photograph of Mask Aligner for photolithography……...……...……...28

Fig. 3.5 The photograph of E-Gun Evaporator System…………….………………..39

Fig. 3.6 XP SU8-3050 spin speed curve………………………………….…………30

Fig. 3.7 Concept of AFM and the optical lever………………………………………32

Fig. 3.8 Schematic diagram of scanning electron microscope………………….……33

Fig. 3.9 Schematic diagram of Hitachi S-4800 SEM……………………………......34

Fig. 3.10 The schematic diagram of the specific vacuum system……………………35

Fig. 3.11 The schematic of ionization gauge……………….……………………......38

Fig. 3.12 Photograph of pulse DC controller and DC power supply………………...40

Fig. 4.1 The cross-section of the square-shape interdigitated electrode microplasma device…………………………………………………………………………...42

Fig. 4.2 The hexagon-shaped interdigitated electrode microplasma device. (a) cross-section with a tilt angle (b) two electrodes confined to the patterned shape (c) cross-section of the dielectric layer and electrode (d)surface morphology of HfO_2………………43

Fig. 4.3 The different patterns of the interdigitated electrode microplasma device. (a) circle-shaped (b) diamond-shaped (c) square-shaped and (d) star-shaped…………...44

Fig. 4.4 The photograph of the fabricated device with the electric wire……………..45

Fig. 4.5 The margin of the firing voltage and the minimum sustain voltage for the interdigitated electrode micro-plasma device with different bipolar voltage waveform frequency of (a) 10, (b) 14.3 and (c) 25 kHz in neon gas at pressure from 300 to 800 Torr……………………………………………………………………………47

Fig. 4.6 The ignition voltage for the interdigitated electrode micro-plasma device with different bipolar voltage waveform frequencies in neon gas at pressure 300 to 800 Torr……………………………………………………………………………48

Fig. 4.7 The firing voltage for the interdigitated electrode micro-plasma device with different dielectric layer thickness in neon gas at pressure from 300 to 800 Torr…...49

Fig. 4.8 The equivalent circuit model to estimate the capacitance of the interdigitated electrode micro-plasma device………………………………………………………50

Fig. 4.9 The ignition voltage for the interdigitated electrode micro-plasma device in pure neon and argon gas at pressure from 300 to 800 Torr…………………………..51

Fig. 4.10 The characteristics of firing voltage and different concentrations of argon gas for the interdigitated micro-plasma device with bipolar voltage waveform frequency of 10 kHz at pressure from 300 to 800 Torr………………………………52

Fig. 4.11 Photograph of the 5x5 arrays of the interdigitated micro-plasma device with a hexagonal structure operating in 300 Torr of neon gas……………………………53

Fig. 4.12 Photograph of the 5x5 arrays of the microplasma device with a diamond structure operating in 300 Torr of (a) neon gas, (b) neon(99%)-argon(1%), and (c) neon(99%)-argon(5%) mixtures……………………………………………………...54

Chapter 1

Introduction

1.1 Micro-plasma Devices

The realm of micro-plasmas can be traced back to a publication by A. D. White in 1959 [1], but also has its roots in the development of the first plasma display panel (PDP) by Bitzer and Slottow in 1966 [2]. More recently work by Schoenbach et al. [3] and Frame et al. [4] have renewed interest in the study of micro-plasmas. Because of their unique electrical and optical properties, micro-plasma devices have been investigated and pursued worldwide [5]-[12]. Much of the interest in micro-plasma devices results from generating efficient vacuum ultraviolet (VUV) to visible radiation.

For past decade, the field of micro-electrical mechanical systems (MEMS) processing technologies offers the key advantages, including small size scales, low mass, low volume, and fast response time. The reduction of the dimensions of a conventional plasma devices afforded by micro-electrical mechanical systems (MEMS), thereby confining the plasma to macroscopic volumes, has given birth to an entirely new area of plasma physics. These devices are known as micro-plasmas and could be the solution for the sequential driving liquid crystal display backlighting, high resolution plasma display panels, environmental sensors, lighting systems, and biomedical systems. A variety of electrode configurations and microcavity cross-sectional geometries have been explored as the following subsections.

1.1.1 Cylindrical Cathode Structure

Hallow cathode discharges are gas discharges between a cathode with a hole and an anode of arbitrary shape. For about 100 years, hallow cathode discharges have been widely used for a variety of applications [13]-[15]. Comparing with a conventional glow discharge between parallel electrodes, shown in *Fig. 1.1*, the hollow cathode geometry is characterized by higher current densities and larger concentrations of high-energy electrons. These properties are preserved even at high pressures simply by scaling the hollow cathode appropriately. These simplest devices of the hollow cathode structure consist of an insulator sandwiched between anode and cathode. *Fig. 1.2* shows qualitatively the three most common micro-plasma geometries. Most of the other micro-plasma geometries can be viewed as a perturbation of one of these three. *Fig. 1.2(a)* has a hole through the anode and insulator. *Fig. 1.2(b)* has a hole through the anode and insulator but also has a cavity machined into the cathode. This structure is typical of hollow cathode discharge. *Fig. 1.2(c)* has a cavity through the entire stack and has a termed a “flow-through” device because it allows for the continuous flow of gas through the plasma.

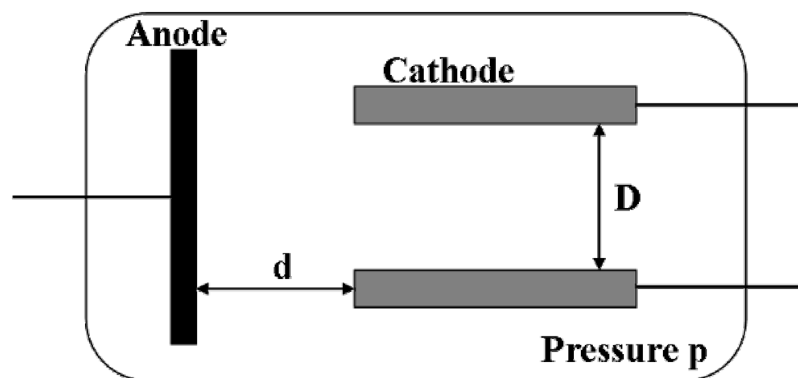

Fig. 1.1. General diagram of a macroscopic hollow cathode discharge device.

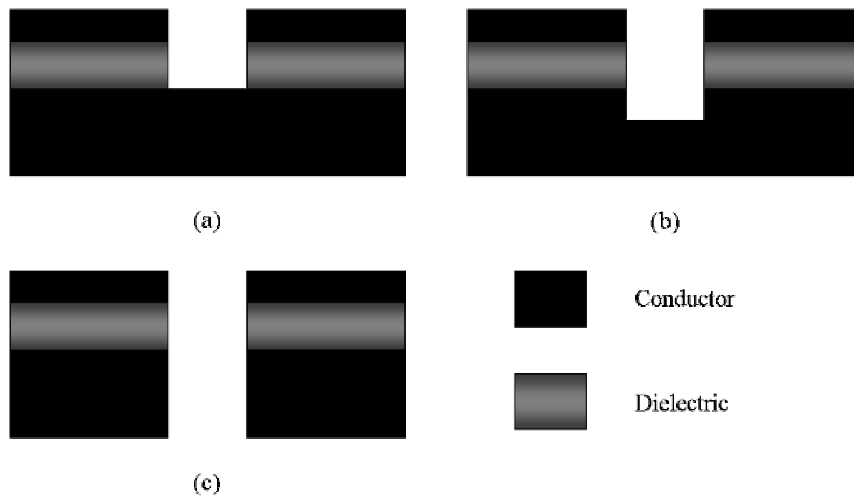

Fig. 1.2. Three typical hollow cathode micro-plasma geometries.

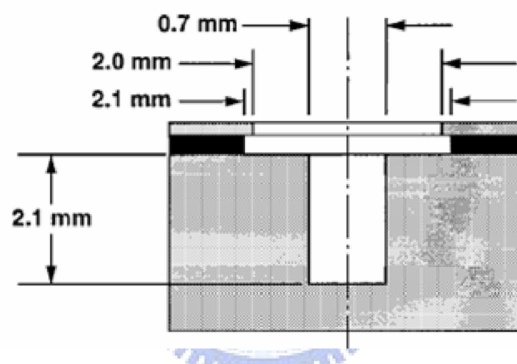

Fig. 1.3. Micro-plasma geometry with cylindrical hollow cathode and anode, separated by a mica insulator.

In 1996, Schoenbach et al. developed "Microhollow cathode discharge" [3]. The device, shown in *Fig. 1.3*, consists of a cylindrical hole in molybdenum of 0.7 mm diameter and 2.1 mm depth. The cathode is separated by a 0.25 mm mica spacer from a ring-shaped anode of 2 mm inside diameter. In addition, direct current (DC) voltages of up to 600 V and pulsed voltages of up to 800 V with 1 ms duration were applied. The operating pressure is up to 100 Torr in argon gas. Reducing the hole diameter down to 200-400 μm is developed by Frame et al. [4] in silicon and their operation in neon and nitrogen. *Fig. 1.4* is a schematic diagram of a representative

device. The discharge can be obtained for neon pressure up to 600 Torr with smaller hole diameter. In other version developed by Biborosch et al. in 1999 term "Microdischarges with plane cathodes" [16], discharges with plane and hollow cathodes were realized in a closed geometry by changing the polarity of the electrodes, as shown in *Fig. 1.5*.

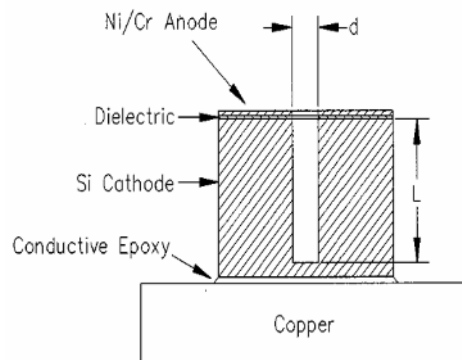

Fig. 1.4. Diagram a single micro-plasma device in silicon.

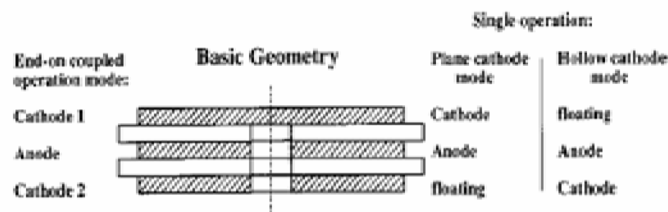

Fig. 1.5. Plane and hollow cathode configuration implemented by external wiring within the same geometry.

1.1.2 Pyramidal Cathode Structure

Micro-discharge devices fabricated in silicon represent a new family of sources [3], [17]-[23]. Silicon-based devices are of particular interest because of the likelihood for integration with electronic and electro-optical devices as well as the

breadth of processing options that are available. The silicon micro-plasma devices having inverted pyramidal cathodes is developed by laboratory for optical physics and engineering in university of Illinois at Urbana-Champaign. The operation of micro-plasma devices having inverted, square pyramidal silicon cathode is shown in *Fig. 1.6*. The devices as small as 50 μm×50 μm and 35 μm in depth have been fabricated to date by conventional lithographic techniques and chemical processing techniques, and operating at gas pressure above atmospheric pressure. Also, the applications of the device have been researched in variety of rare gas including argon, neon and xenon.

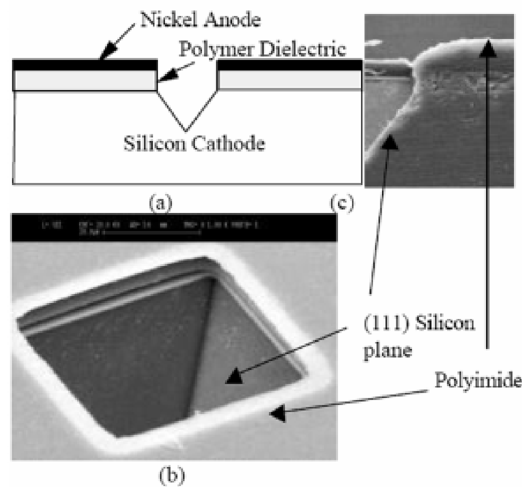

Fig. 1.6. Micro-plasma geometry with pyramidal cavity: (a) Cross-section diagram; (b) SEM micrograph of a single device; (c) SEM micrograph of the device cross-section, the particulate in the figure result from dicing.

1.2 Applications of Micro-plasma Devices

The rapid growth of the micro-plasma devices is widely used in many areas, including biomedical applications, displays, and other applications such as high power

lasers, novel plasma processing applications, electromagnetic (EM) absorbers and reflectors, remediation of gaseous pollutants, excimer lamps and other non-coherent vacuum-ultraviolet (VUV) light sources. Some applications of micro-plasma devices will be given in the following.

1.2.1 Micro-plasmas for biomedical and environmental applications

Depending on the noble gas, the micro-plasmas can sterilize germs by emitting light in the range from vacuum ultra-violent (VUV) to visible light. The discharge can kill germs for instrument or surface disinfection. Consequently, non-thermal plasmas have been applied to environmental applications such as the remediation of gaseous waste streams [24]. Areas of application for non-thermal plasmas in the environmental field include NO_x and SO_x remediation and the destruction of volatile organic compounds (VOCs) [25]. High energy electron beams, corona discharges, dielectric barrier discharges (DBDs) and various surface-type discharges, sometimes in conjunction with a packed bed of ferroelectric pellets, have been the most widely utilized discharge configurations for the generation of non-thermal plasmas for environmental applications.

1.2.2 Micro-plasmas for display applications

Plasma display panel (PDP) is a self-emission flat panel display where the visible light is created by exciting phosphors. The plasma discharge between two flat panels of glass generates ultra-violent (UV) light to excite phosphors. Because of self-emission, plasma display panel (PDP) which is contrary to the backlights of an AMLCD contains no mercury. An inert mixture of noble gases (neon and xenon) is

used instead. There are many advantages such as, wide viewing angle, high contrast ratio and large size panel. Therefore, the micro-plasmas can afford high resolution for high-definition television (HDTV), where cinema-quality pictures are presented on a wide screen.

1.2.3 Micro-plasmas for other applications

In semiconductor process, micro-plasmas covered widely such as sputtering, plasma-enhanced chemical vapor deposition (PECVD) and miniature inductively coupled plasmas (ICPs). In addition, the sensors and the light sources such as high power laser and excimer lamps have been reported [26]-[28]. There are still a lot of applications that people are researching worldwide. Therefore, the micro-plasma devices are very attractive to many areas.

E S A 1896

1.3 Motivation and Objective of this Thesis

The exiting micro-plasma devices have revealed that dimensional control cannot keep consistently accurate by the drilling method, shown in *Fig.1.7* [3]-[5], [8]. In addition, such a process for the micro-cavity fabrication is not feasible to make large size panel and hard to make stable glow discharge. Recently, semiconductor technology has contributed the micro-plasma fabrication process to achieve a realm of device possibilities. Furthermore, the low cost assembly of large micro-plasma device arrays has been realized [20]-[23]. Also, a novel micro-plasma structure, interdigitated electrode microplasma device, was proposed by Sung-O Kim [29][30]. However, the photo-definable glass as a barrier rib is incompact enough with the substrate. The gap between glass and substrate will influence the discharge phenomena. Therefore,

utilizing the thick photoresist (XP SU-8 3050) as a barrier rib was proposed to avoid a misfiring plasma between barrier rib and substrate. Because the thick photoresist is spun-coated on the substrate, it can perfectly generate the thick barrier rib on the substrate. In addition, this technology affords the opportunity to realize any geometry and high resolution patterns by the lithographic techniques.

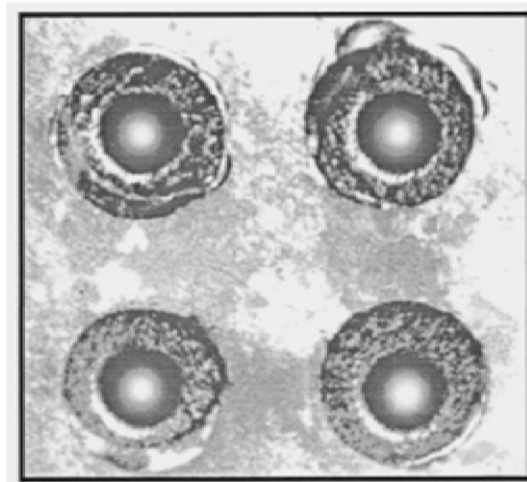

Fig. 1.7. The photograph of micro-plasma geometry with cylindrical hollow cathode by drilling method.

1.4 Arrangement of this Thesis

The thesis is arranged as following: the principles and the characteristic of gas discharge will be described in ***Chapter 2***. In ***Chapter 3***, the fabrication process of proposed device is described. Besides, the measurement equipments used to characterize the device are illustrated. In ***Chapter 4***, the results including ignition voltage, voltage margin and the glow images operating in neon and argon gas are presented and discussed. The conclusion of the thesis and the future work are given in ***Chapter 5***.

Chapter 2

Principle

2.1 Introduction

A better concept of micro-plasma devices can be gained by considering more conventional plasma phenomena. This chapter provides some background information on describing the behavior of gas discharges. Some background is given on breakdown in gas and glow discharges. Also, the importance of *Paschen's law* is explored and its effect on the operation of gas discharges at this thesis is discussed.

2.2 Plasma

Generally, the term "plasma" is used to describe a partially or completely ionized gas containing electrons, ions and neutrals. Although there is always a small degree of ionization in any gas, a stricter definition of the plasma is "a quasi-neutral gas of charged and neutral particles which exhibits collective behavior" [31]. Quasi neutrality refers to the characteristic that positive and negative space charges balance in a given volume such that overall, the plasma is considered to be electrically neutral. The collective behavior of the plasma is result from the Coulomb forces that are long range and cause remote regions to interact with one another.

In *Fig. 2.1*, Micro-plasmas show a new class of the plasma whose properties fall somewhere between those of glow discharge and arcs. These two types of processing plasma are characterized to low-pressure glow discharges and high-pressure arcs.

However, the low electron temperature and non-equilibrium make them more similar to glow discharges. As a result, they are often referred to as a “high pressure glow discharges”.

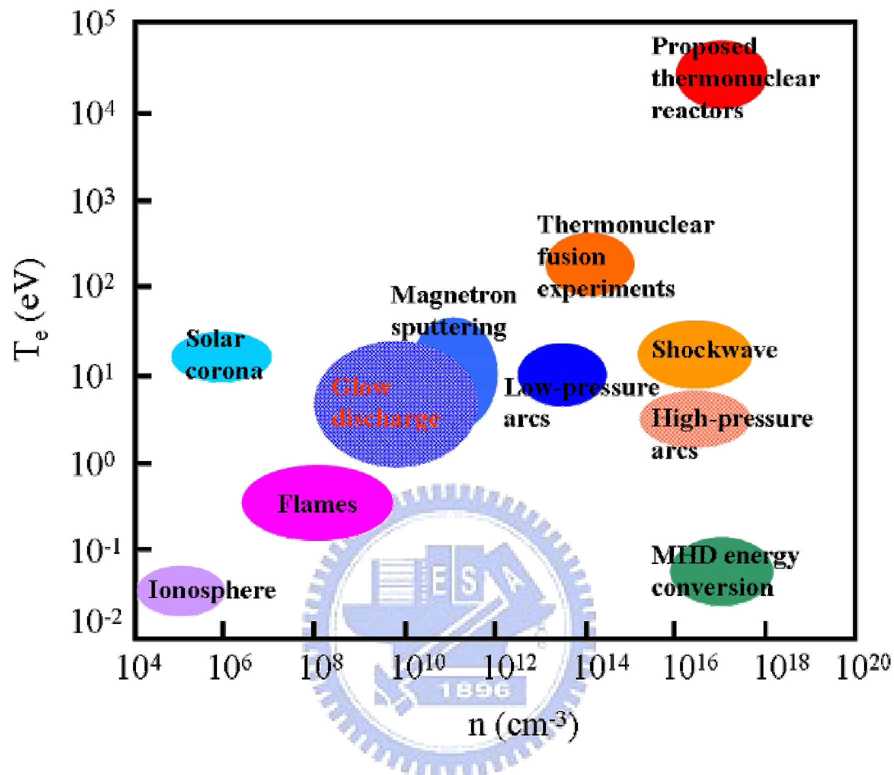

Fig. 2.1. Space and laboratory plasmas classified by their electron temperature, T_e, and charged particle density, n [32].

2.3 Gas Discharges

2.3.1 Gas Breakdown and Paschen's Law

The phenomenon of gas breakdown is considered as the transition from insulating state to conducting state. The associated voltage required to cause the transition is referred to as the breakdown voltage. Current flows between the electrodes via the movement of charged particles (ions and electrons) to and from the electrodes. When the electrons are energetic enough to dissociate the gas through impact to create ions, formation of a gas discharge occurs. The average electron temperature, T_e, is generally less than breakdown energy required for ionization. Ionization processes are possible because electrons have a distribution of energies [32]. If we assume a Maxwellian distribution at the average electron temperature, T_e, the electron energy distribution function will be of the form [32]:

$$g(\varepsilon) = \sqrt{\varepsilon}\exp(-\frac{\varepsilon}{T_e}) \tag{2.1}$$

where ε is the electron energy. From the graphical depiction of Eq. 2.1 in *Fig 2.2*, the distribution shows a maximum corresponding to $T_e/2$ and a tail at higher energies. Electrons in the high-energy distribution are responsible for ionization processes that create and sustain the plasma. For non-Maxwellian plasmas, the tail of the distribution may be higher or lower than that shown in *Fig. 2.2* because of electron heating or collision processes. If the plasma is to be sustained after breakdown, there must be a mechanism for the generation of electrodes and ions to replace the ones lost to the electrodes.

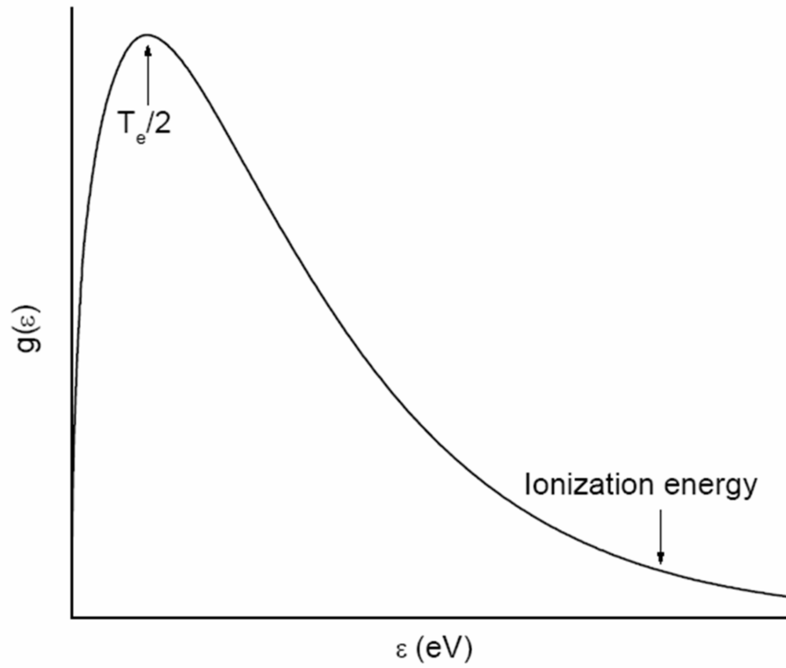

Fig. 2.2. Electron energy distribution in a weakly ionized gas, assuming a Maxwellian distribution at the average electron temperature, T_e.

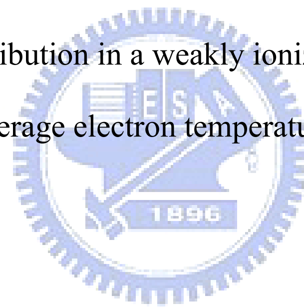

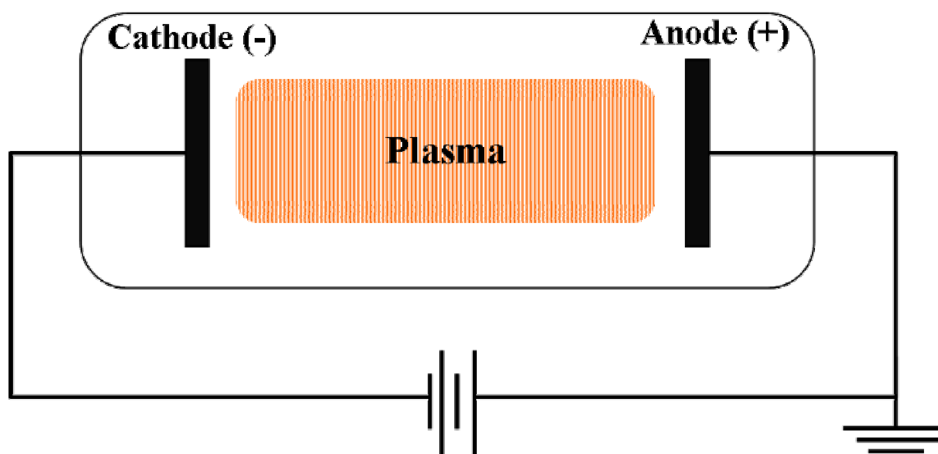

Fig. 2.3. The diagram of the plane parallel electrode for producing a direct current (DC) glow discharge.

The simplest configuration employed for striking a gas discharge is plane parallel electrode, a cathode and an anode, separated by a distance of d, as illustrated in *Fig. 2.3*. The interelectrode space is filled with a noble gas at a pressure of p. The volume processes are defined by collisions between energetic electrons and neutrals that from an ion, and as a result, another electron. Thus the change in the number of electrons along an element of length dx, is proportional to the number of electrons n_e at x. This equation and its solution are given by :

$$dn_e = \alpha n_e dx \tag{2.2}$$

$$n_e(x) = n_e(0)\exp(\alpha x) \tag{2.3}$$

where α is an ionization coefficient which is known as the first Townsend coefficient. By integrating between $x=0$ and $x=d$ we obtain for the number of electrons n_d at d or the current i_d at d :

$$\frac{n_d}{n_0} = \frac{i_d}{i_0} = \exp(\alpha d) \tag{2.4}$$

where n_0 is the the number of electrons at $x=0$ and i_0 the current produced by irradiation of the cathode. When an energetic ion strikes the cathode, electrons are liberated from the cathode surface as a result of secondary electron emission, γ, defined as the probability of a secondary electron generation on the cathode by an ion impact. An electron generated from the cathode produces $\exp(\alpha d)-1$ positive ions in the interelectrode space. We neglected the electron losses here due to recombination and attachment to electronegative molecules. Electron–ion

recombination was neglected because the ionization degree is very low during the breakdown; attachment processes important in electronegative gases will be especially discussed below. All the $\exp(\alpha d)-1$ positive ions produced in the gap per electron move back to the cathode, and altogether strike out $\gamma[\exp(\alpha d)-1]$ electrons from the cathode in the process of secondary electron emission. The current in the gap is non-self-sustained as long as $\gamma[\exp(\alpha d)-1]$ is less than one because positive ions generated by electron avalanche must produce at least one electron to start a new avalanche. As soon as the electric field becomes high enough the transition to self-sustained current (the breakdown) takes place. Thus, the simplest breakdown condition in the gap can be expressed as :

$$\gamma[\exp(\alpha d)-1]=1 \tag{2.5}$$

It is possible to derive relations for the breakdown electric field based on Eq. 2.5 by rewriting the ionization coefficient α, relating the similarity parameters α/p and E/p.

$$\frac{\alpha}{p}=A\exp(-\frac{B}{E/p}) \tag{2.6}$$

where A and B are published values for different operating characteristics, E is the electric field and p is the noble gas pressure. Combination of Eq. 2.5 and 2.6 gives the following convenient formula for the breakdown voltage :

$$V_B=\frac{B\times pd}{\ln\left[\frac{A}{\ln(1+1/\gamma)}\right]+\ln(pd)} \tag{2.7}$$

This relationship is referred as *Paschen's law*. The law essentially states that the breakdown characteristics of a gap are a function (generally not linear) of the product of the gas pressure and the gap length [33]. The experimental Paschen's curves for different gases are illustrated in *Fig. 2.4*. These curves have a minimum voltage point, corresponding to the easiest breakdown conditions. In the case where *pd* is small, low pressure or narrow gaps, the number of ionizing collisions is minimized through a lack of available neutrals or a short path length over which a collision can occur. Therefore, the curve rises rapidly on the side left of the minimum. The right side of the curve scales almost linearly with *pd* because the probability that an electron will undergo an ionizing collision is still high.

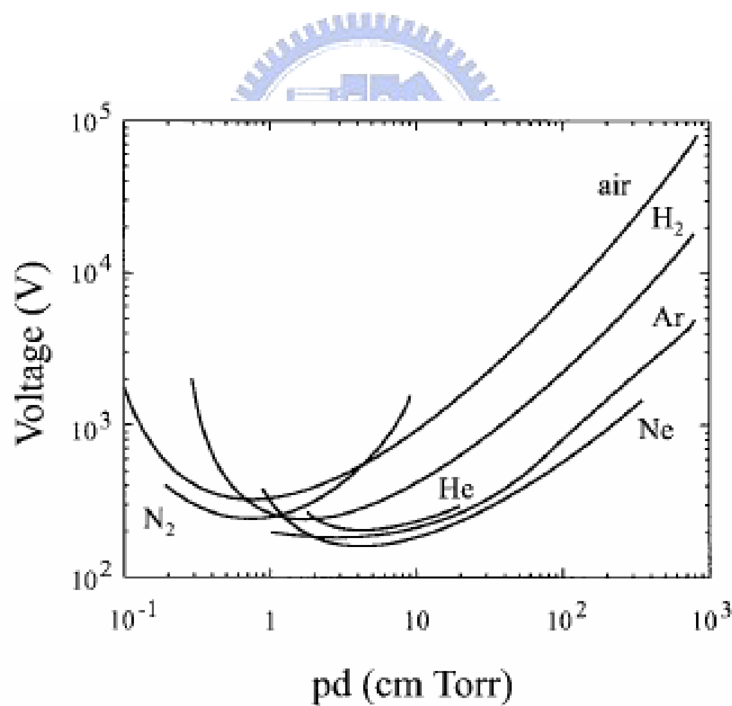

Fig. 2.4. The experimental Paschen's curves for different gases.

2.3.2 Glow Discharges

The name of glow discharge is the phenomenon that plasma is luminous and depends on the geometry of the electrodes and the vessel, the gas used, the electrode material. When breakdown occurs, the gas suddenly becomes conductive. The current and voltage in the gas discharge vary resulting changing supply voltage. These parameters can be measured to obtain a voltage-current (V-I) characteristic for a discharge as illustrated in *Fig. 2.5*. In addition, current is limited through the discharge by using an external ballast resistor.

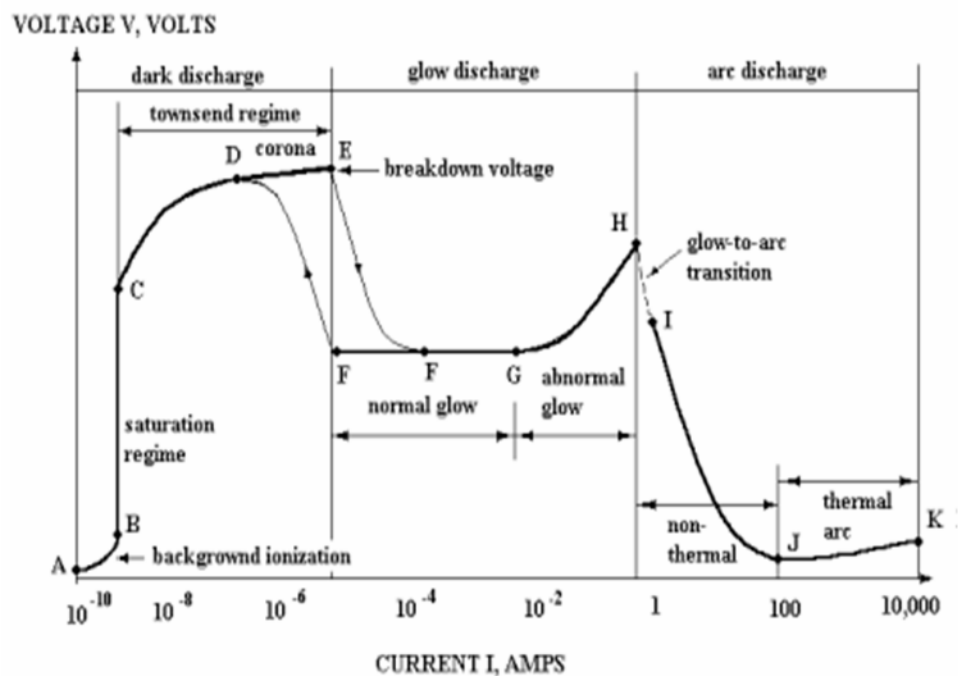

Fig. 2.5. Voltage-current (V-I) characteristic for a discharge.

Three general regions can be identified on the diagram above, the dark discharge (Townsend region), the glow discharge and the arc discharge. Because the discharge remains invisible to the eye except for corona discharge and the breakdown itself, the regime between A and E on the voltage-current characteristic is termed a dark

discharge. The electric field sweeps out the ions and electrons created by ionization from background radiation during the *background ionization*. The ions and electrons migrate to the electrodes in the applied electric field producing a weak electric current. Increasing voltage results in an increasing fraction of these ions and electrons. If the voltage between the electrodes is increased far enough, eventually all the available electrons and ions are swept away, and the current saturates. The regime is named the *saturation region* because the current remain constant while the voltage is increased. After the voltage across the *saturation region*, the current will rise exponentially. The electric field is now high enough so the electrons initially present in the gas can acquire enough energy before reaching the anode to ionize a neutral atom. As the electric field becomes even stronger, the secondary electron may also ionize another neutral atom leading to an avalanche of electron and ion production. The regime of exponentially increasing current is called the *Townsend discharge*. The *Corona discharge* occurs in the regime of *Townsend discharge* because of high electric field near sharp points, edges, or wires in gases prior to electrical breakdown. If the coronal currents are high enough, *corona discharge* can be technically "glow discharges", visible to the eye. For low currents, the entire corona is dark, as appropriate for the dark discharge. After the breakdown, the gas enters the *normal glow* regime, which the voltage is almost independent of the current over several orders of magnitude in the discharge current. The electrode current density is independent of the total current in this regime. This means that the plasma is in contact with only a small part of the cathode surface at low currents. As the current is increased, the fraction of the cathode occupied by the plasma increases until plasma covers the entire cathode surface. When the cathode is completely covered by the plasma, the current is increased by increasing the voltage in order to force the cathode current density above its natural value and provide the desired current. The regime which has the positive slope of

current-voltage curve is so-called the *abnormal discharge*. The discharge maintains itself at considerably lower currents and current densities and only then makes a transition back to *Townsend discharge* regime. Further increase in the current will result in a sudden drop in voltage and the discharge will undergo a *glow-to-arc transition*. After transition of the discharge is an *arc discharge* where the discharge voltage decreases as the current increases, until large currents are achieved at a low voltage, and after that the voltage increases slowly as the current increases.

The glow can be produced by applying a potential difference in a gas between two electrodes. The potential drops rapidly close to the cathode, vary slowly in the plasma, and change again close to the anode. The voltage distribution in a dc glow discharge process is shown in *Fig. 2.6*. The electric fields between the gaps are restricted to sheath at each of electrodes. The sheath fields are such as to repel electrons trying to reach either electrode. Electrons originating at the cathode will be accelerated, collide, transfer energy, leave by diffusion and recombination, slow by the anode and get transferred into the outside circuit. The luminous glow is produced because the electrons have enough energy to generate visible light by excitation collisions. Since there is a continuous loss of electrons, there must be an equal degree of ionization going on to maintain the steady state. The energy is being continuously transferred out of the discharge and hence the energy balance must be satisfied also. Simplistically, the electrons absorb energy from the field, accelerate, ionize some atoms, and the process becomes continuous. Additional electrons are produced by secondary emission from the cathode. These are very important to maintain a sustainable discharge.

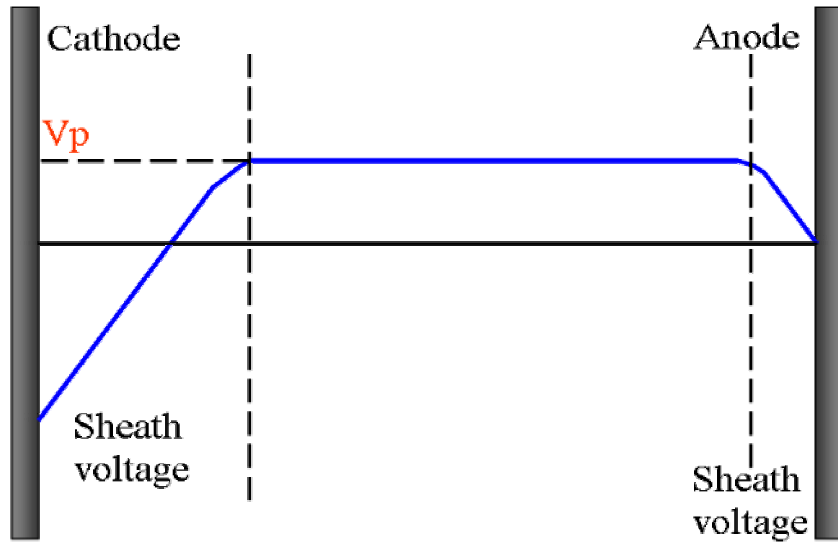

Fig. 2.6. The potential distribution in a dc glow discharge process.

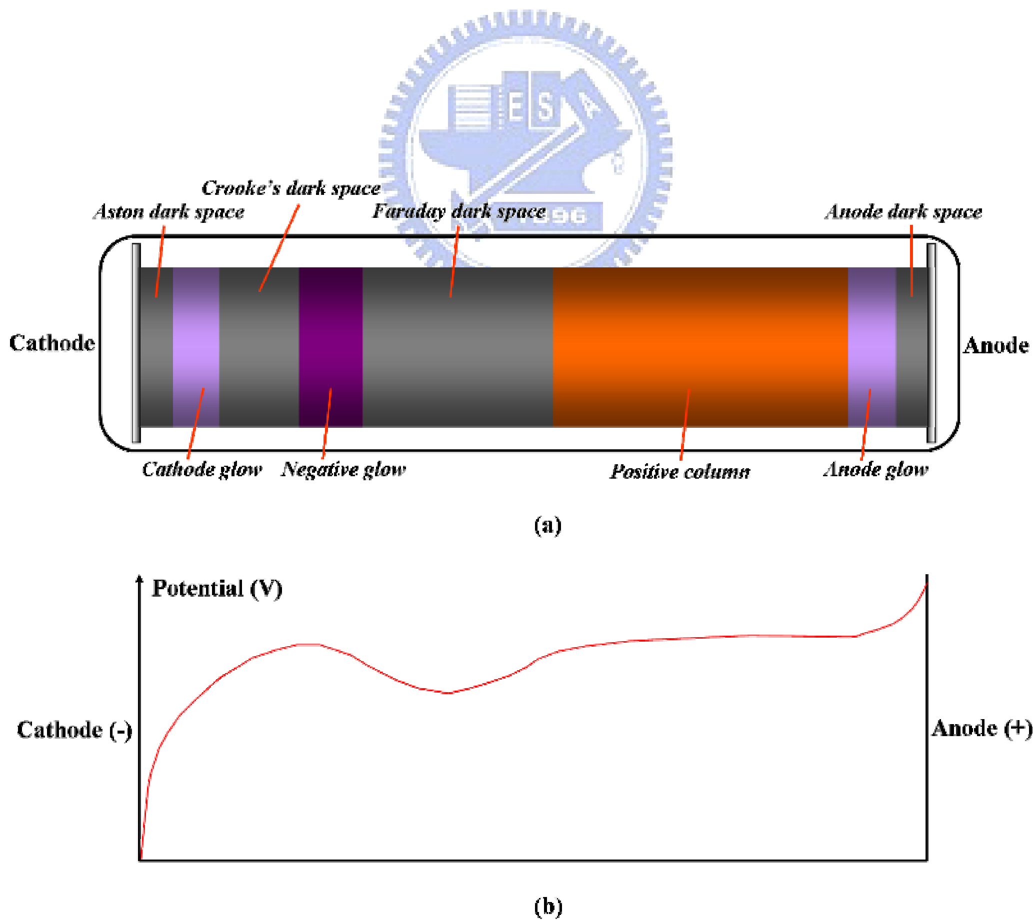

Fig. 2.7. The spatial distribution of (a) the luminous regions in a typical discharge and (b) the electric field.

Unlike Townsend or arc discharge, the glow discharge is characterized by distinct regions with large variations in electric field [34]. The approximate appearance of the different luminous regions is shown in *Fig. 2.7(a)*. Also shown for reference is the associated potential distribution between cathode and anode in *Fig. 2.7(b)*. Three basic regions are described below, the cathode region, the glow regions and the anode region. The length of the *cathode region* is from the cathode surface to the boundary of the *negative glow*. Most of the potential drop across the cathode and anode occur between the cathode and the negative glow. The energies of electrons accelerated in this region are high enough to produce ionization and avalanching in the regions to the right of the right of the *negative glow*. The electrons are accelerated from the cathode to *Aston Dark Space* which is a thin regime with a strong electrical field. This regime has a negative space charge, meaning that stray initial electrons together with the secondary electrons from the cathode outnumber the ions in this regime. The electrons are too low density and/or energy to excite the gas, so it appears dark. The next regime to right of *Aston dark space* is *cathode glow*. The electrons are energetic enough to excite the neutral atoms they collide with. In addition, the *cathode glow* has a relatively high ion density. The cathode dark space that is to the right of the *cathode glow* has moderate electric field, a positive space charge and a relatively high ion density. These fine-structured regions make up what is known as *Crooke's dark space* which is commonly referred to as the cathode fall or sheath. The brightest intensity of the entire discharge names *negative glow*. The *negative glow* has relatively low electric field, long, compared to the cathode glow and is the most intense on the cathode side. Electrons carry almost the entire current in the negative glow region. Electrons that have been accelerated in the cathode region to high speeds produce ionization, and slower electrons that have had inelastic collisions already produce excitations. These slower electrons are responsible for the negative glow. The

electron number density in the negative glow is about 10^{16} electrons/m^3. Before reaching the *positive column*, the electrons lose their energy through more collisions in the *Faraday dark space*. The electron density decreases by recombination and diffusion to the walls. Furthermore, the net space charge is very low and the electric field is small. The uniform electric field in the *positive column* continually accelerates the electrons, which, in turn, undergo decelerating collisions. In the regime, small electric field is typically 1 V/cm. The electric field is just large enough to maintain the degree of ionization at its cathode end. The electron number density is about 10^{15} to 10^{16} electrons/m^3 in the *positive column*, and the electron temperature of 1 to 2 eV. A thin sheath also exists near the anode with a similar structure to the cathode fall made-up of the *anode glow* and *anode dark space*. The voltage drop in this region is significantly smaller than near the cathode and plays little role in the discharge dynamics. *Anode glow* is slightly brighter than positive column. This is the boundary of the anode sheath. The *anode dark space* between the anode glow and the anode is the anode sheath. It has negative space charge due to electrons traveling from the positive column to the anode. There is a higher electric field than the positive column. The anode pulls electrons out of the positive column and acts like a Langmuir probe in electron saturation.

2.4 Penning Effect

A gas mixture consists of a rare gas containing impurity atoms possibly at very low concentrations. The impurity atoms have an ionization potential V_{ion} which is lower than or equal to the metastable potential V_{meta} of the minority nobles gas. The Penning effect in a gas mixture is the ionization by charge transfer (charge exchange)

during collision between a metastable atom and a neutral atom which decreases the average energy to form an ion pair, e.g.

$$Ne^{*} + Ar \rightarrow Ne + Ar^{+} + e \qquad (2.8)$$

In a glow discharge, the Penning effect results in an increase of the ionization coefficient (Townsend first coefficient). In other hand, the breakdown potential and the cathode fall potential are decreased. The ionization and metastable energies of the rare gas are listed in Table 2.1.

Table 2.1 The ionization and metastable energies of the rare gas.

	Ionization and Metastable energies	
Gas	***Ionization energy (eV)***	***Metastable energy (eV)***
He	24.6	19.8, 20.6
Ne	21.6	16.6, 16.7
Ar	15.8	11.5, 11.7
Kr	14	9.9, 10.5
Xe	12.1	8.3, 9.4

Chapter 3

Fabrication and Measurement Instruments

3.1 Introduction

The interdigitated electrode micro-plasma device will be demonstrated in this chapter. The embodiment including the fabrication processes, technologies and instruments which are available to develop the structure of interdigitated electrode micro-plasma device will be described in the following sections. First, the semiconductor process including wet bench, furnace, spin coating, exposure, develop, sputter, lift-off and evaporate will be used. Besides, the features of the fabricated device were measured by typical semiconductor measurement systems, such as optical microscope, atomic force microscope (AFM), scanning electron microscope (SEM). In addition, the performance, such as ignition voltage, voltage margin and glow images were characterized in a specific vacuum system including charge-couple device (CCD) camera and pulse DC controller. The mentioned instruments mentioned above will be illustrated in this chapter.

3.2 Semiconductor Fabrication Process

The detail fabrication processes are listed below and the flow chart is shown in *Fig. 3.1*.

(a) **Substrate Cleaning**

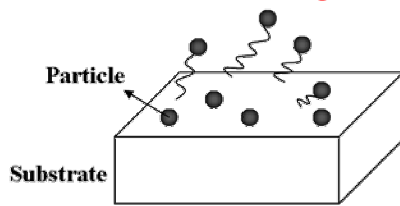

(b) **Silicon Oxide Growth**

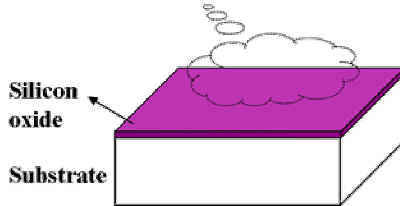

(c) **UV Exposure**

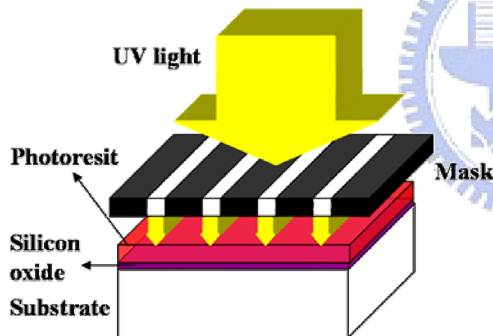

Metal Deposition

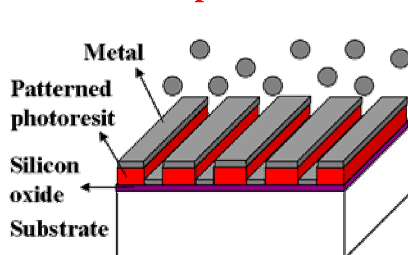

Lift-Off

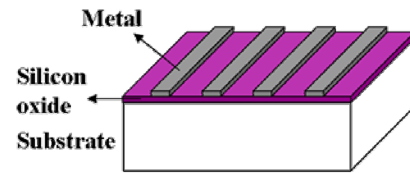

(d) **Dielectric Layer Deposition**

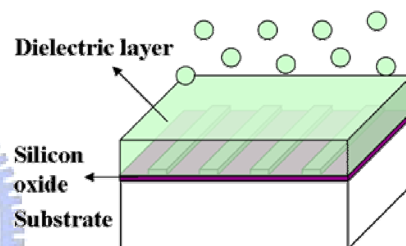

(e) **Barrier Rib Formation**

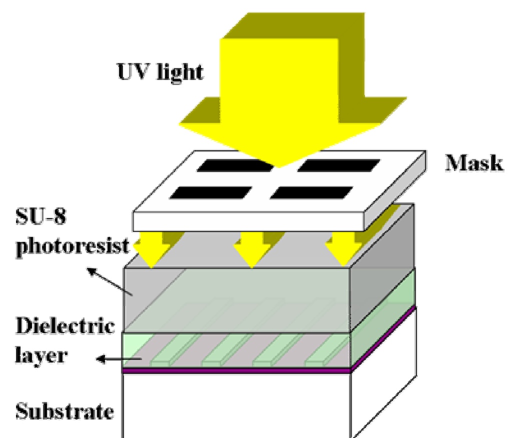

Fabricated Device

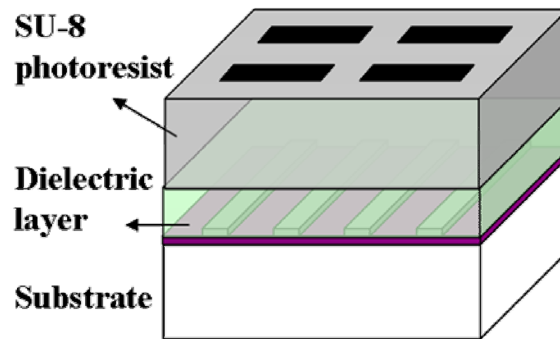

Fig. 3.1. The flow chart of fabrication process for micro-plasma device (a) substrate cleaning (b) silicon oxide growth (c) metal deposition (d) dielectric layer deposition (e) barrier rib formation.

a. Substrate Cleaning:

First of all, silicon wafers were cleaned by RCA clean in wet bench, shown in *Fig. 3.2*. The RCA clean is the industry standard for removing contaminants from silicon wafer. Werner Kern developed the basic procedure at RCA (Radio Corporation of America) laboratories in 1960’s. As shown in *Table 3.1*, the main purpose for this procedure is removing organic residue and films from silicon wafers. The decontamination works based on sequential oxidative desorption and complexing with H_2O-NH_4OH-H_2O_2 (called “standard clean-1”, SC-1) at 75~85 °C. A second standard clean (SC-2) is often used H_2O-HCl-H_2O_2 at 75~85 °C to further clean the surface. SC-1 is used to remove the organic residues from silicon wafer. In the process, it oxidizes the silicon and has a thin oxide on the surface of the wafer which should be removed is a pure silicon surface is desired.

Fig. 3.2. The photograph of Wet Bench for silicon cleaning.

Table 3.1 The RCA clean procedure.

RCA Clean Steps		
1.	DI water rinse, 5 min	
2.	$H_2SO_4 : H_2O_2 = 3:1$	Organic Clean
3.	DI water rinse, 5 min	
4.	$HF : H_2O = 1:100$	Chemical oxide Strip
5.	DI water rinse, 5 min	
6.	$NH_4OH : H_2O_2 : H_2O = 1:4:20$ (SC-1), 10 min (75~85 °C)	Particle Clean
7.	DI water rinse, 5 min	
8.	$HCl : H_2O_2 : H_2O = 1:1:6$ (SC-2), 10 min (75~85 °C)	Ionic Clean
9.	DI water rinse, 5 min	
10.	$HF : H_2O = 1:100$	Chemical oxide Strip
11.	DI water rinse, 5 min	
12.	Spinner	Dry wafers

1896

b. Silicon Oxide Growth:

Because silicon wafer is a semiconductor, the electrode formed on the surface will influence the discharge properties without a buffer layer. In order to avoid discharge between electrode and silicon wafer, a quite thick silicon oxide (about 1 μm) was grown on the surface as a buffer layer. The buffer layer was grown at 1100 °C using both thermal wet and dry oxide by Furnace, shown in *Fig. 3.3*.

Fig. 3.3. The photograph of Furnace for thermal oxide.

1896

Table 3.2 The growth of 1 μm silicon oxide for Si (100).

Thermal Oxide Growth (1100 °C)	
Wet oxide	135 minutes
Dry oxide	20 minutes

c. Metal Deposition:

After growing a buffer oxide on the silicon wafer, the electrode was fabricated on the buffer oxide. Firstly, the HMDS is sprayed to increase the adhesion between substrate and photoresist. In the procedure, the positive photoresist (FH-6400) was spin coated on the surface of substrate and then was exposed UV light by Mask Aligner (MJB-3, Karl-Suss), shown in *Fig. 3.4*. Consequently, the pattern on the mask

was transformed to positive photoreisit after developing. The pattern was used to define the geometric feature of electrode layer. The width of the gap between each electrode and electrode are 20 μm and 15 μm, respectively. The metal electrode, chromium (Cr), was evaporated on the substrate with patterned photoresist by E-Gun Evaporation System and then the electrode layer was formed by lift-off technology.

Fig. 3.4. The photograph of Mask Aligner for photolithography.

1896

Table 3.3 The lithography procedure for patterning the electrode.

Lithography Steps	
1. Spray HMDS	In a vacuum oven (150 °C)
2. Spin Coating Photoresit (FH-6400)	1st Spin Speed: 1000 rmp, 10 sec.
	2nd Spin Speed: 3500 rmp, 40 sec.
3. Soft Bake	90 sec. at 90 °C
4. Exposure	40 sec.
5. Development	20~30 sec.
6. After Develop inspection (ADI)	
7. Hard Bake	150 sec. at 120 °C

d. Dielectric Layer Deposition:

In order to make plasma by bipolar voltage waveform, the dielectric layer should be deposited on the electrode. The HfO_2 pellet which is the source material of dielectric layer was evaporated by E-Gun Evaporation System, shown in *Fig. 3.5*. Before evaporating dielectric layer, the electrode pad was shadowed by the vacuum type.

Fig. 3.5. The photograph of E-Gun Evaporator System.

1896

e. Barrier Rib Formation:

After depositing the dielectric layer (HfO_2), the thick photoresist (XP SU-8 3050) was spin coated on the dielectric layer. Finally, the geometric pattern was realized by the lithographic techniques. The detail parameters are shown in *Table 3.1*. In the procedure, the thick photoresist (XP SU-8 3050) was spin coated on the dielectric layer. The first spin speed was 750 rmp for 25 seconds until the thick photoresist (XP SU-8 3050) reaches the edge of the substrate. The second spin speed was 3000 rmp for 40 seconds to obtain the desired thickness, referring to the attached spin speed curve in *Fig. 3.6*. Soft bake the coated substrate in two steps. Firstly increase the temperature from room temperature up to 65°C. Let the substrates at 65 °C for 1 min and then increase up to 90 °C for 15 min. After cooling gradually to the room temperature, the substrate was exposed by UV light for 25 seconds. Consequently, the

pattern on the mask was transformed to the thick photoresit (XP SU-8 3050) after post exposure bake (PEB). The time of post exposure bake (PEB) is 1.5 minutes at 65 °C and then 90 °C for 6 minutes. Developing 8 minutes in SU-8 Developer and rinse with Isopropanol (IPA). Once there is not any white traces the development is then finished. With temperature of 175 °C for 15 minutes, the hard bake was implemented before drying the wafer at the ambient air on a wet bench.

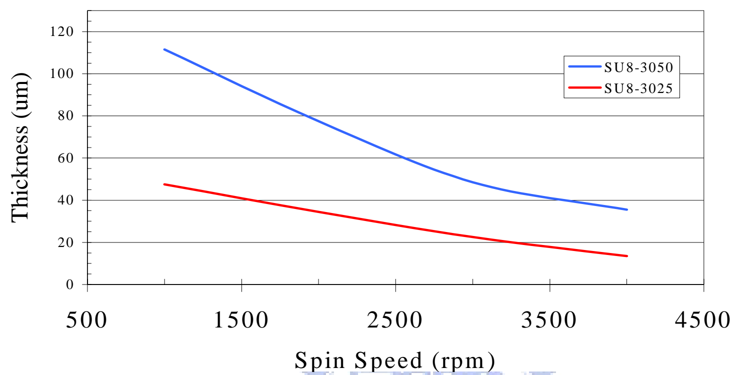

Fig. 3.6. XP SU8-3050 spin speed curve.

Table 3.4 The parameters of XP SU-8 3050 photoresist.

Product	Spin Speed (rpm)	Soft Bake Time	Exposure Time
	1st @ 750 (25 sec.)	1 min @ 65 °C	25 sec.
SU-8	2nd @ 3000 (40 sec.)	15 min @ 90 °C	
3050	PEB Time	Development	Hard Bake Time
	1.5 min @ 65 °C	8 min	15 min @ 175 °C
	6 min @ 90 °C		

3.3 Measurement Instruments

After the fabrication of the interdigitated electrode micro-plasma device, the inspection will be performed to ensure that the fabricated structure agrees with the designed structure. At first, the optical microscope, atomic force microscope (AFM) and scanning electron microscope (SEM) will be introduced. In addition, a specific vacuum system is necessary to characterize the performance of the interdigitated electrode micro-plasma device after the fabrication process. Accordingly, a specific vacuum system, including charge-couple device (CCD) camera and pulse DC controller, will be illustrated in the following.

3.3.1 Atomic Force Microscope (AFM)

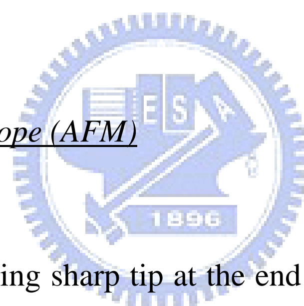
ES A 1896

AFM consists of a scanning sharp tip at the end of a flexible cantilever across a sample surface while maintaining a small, constant force. The tips typically have an end radius of 2 nm to 20 nm, depending on tip type. The scanning motion is conducted by a piezoelectric tube scanner which scans the tip in a raster pattern with respect to the sample (or scans to the sample with respect to the tip). The tip-sample interaction is monitored by reflecting a laser off the back of the cantilever into a split photodiode detector. By detecting the difference in the photodetector output voltages, changes in the cantilever deflection or oscillation amplitude are determined. A schematic diagram of this mechanism is depicted in *Fig. 3.7*.

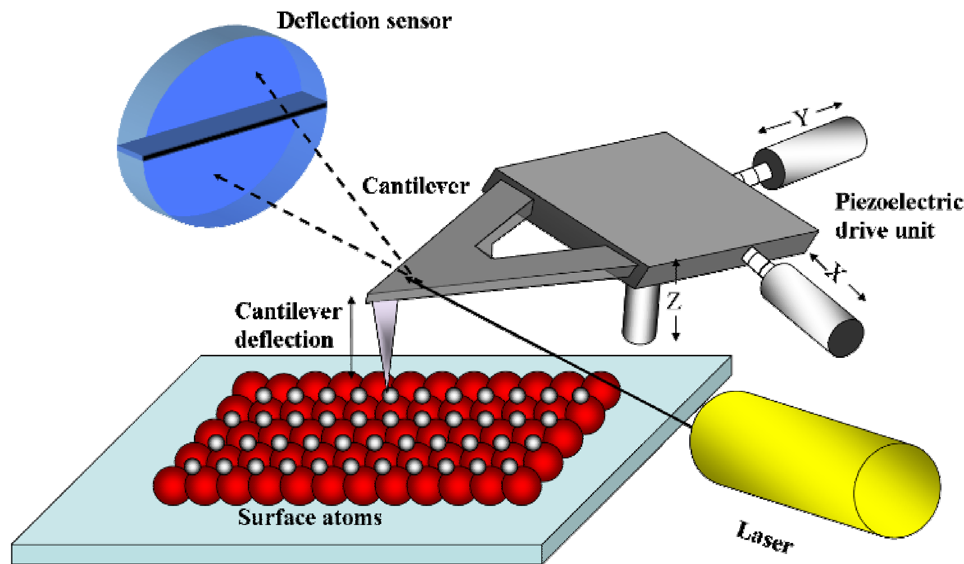

Fig. 3.7. Concept of AFM and the optical lever.

The two most commonly used modes of operation are contact mode AFM and tapping mode AFM, which are conducted in air or liquid environments. Contact mode AFM consists of scanning the probe across a sample surface while monitoring the change in cantilever deflection with the split photodiode detector. A feedback loop maintains a constant cantilever deflection by vertically moving the scanner to maintain a constant photodetector difference signal. The distance the scanner moves vertically at each x, y data point is stored by the computer to form the topographic image of the sample surface. This feedback loop maintains a constant force during imaging, which typically ranges between 0.1 to 100 *nN*.

Tapping mode AFM consists of oscillating the cantilever at its resonance frequency (typically ~300 *kHz*) and lightly "tapping" on the surface during scanning. The laser deflection method is used to detect the root-mean-square (RMS) amplitude of cantilever oscillation. A feedback loop maintains a constant oscillation amplitude by moving the scanner vertically at every x, y data point. Recording this movement forms the topographical image. The advantage of tapping mode over contact mode is

that it eliminates the lateral, shear forces present in contact mode, enabling tapping mode to image soft, fragile, and adhesive surfaces without damaging them, which can be a drawback of contact mode AFM.

3.3.2 Scanning Electron Microscope (SEM)

Scanning electron microscope (SEM) is an essential instrument to measure the accuracy and fidelity of the fabricated devices, as shown in *Fig. 3.8*. Using a series of electromagnetic lenses to focus the accelerated electron beam, the diameter of electron beam can be converged to the dimension of 10^{-3} μm. The secondary electrons are generated where the focused accelerated electrons bombard the sample. Detecting the secondary electrons can determine the location of bombardment. Simultaneously, the focusing electron beam scans the surface of sample, with the aid of scanning coil, to map the feature of measured area, as shown in *Fig. 3.9*. Using SEM, the feature variation of a few angstroms can be observed.

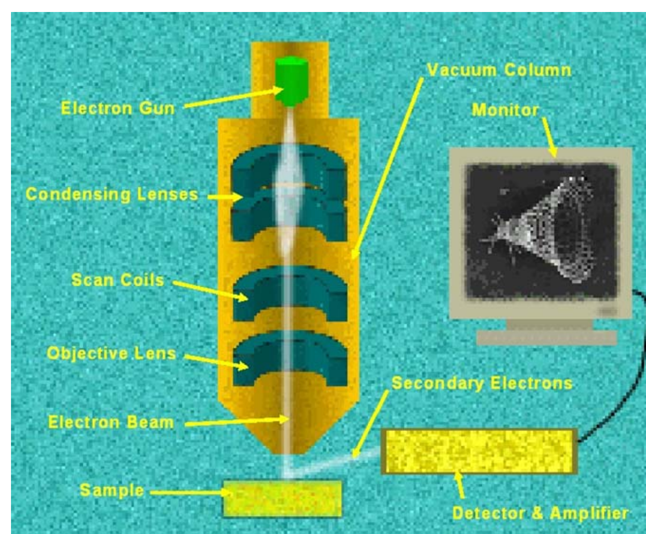

Fig. 3.8. Schematic diagram of scanning electron microscope.

In this thesis, a Hitachi S-4800 SEM was used to measure the features of the interdigitated electrode micro-plasma device. The electrode thickness, dielectric thickness, barrier rib height, aperture size of geometric pattern and cross-section of fabricated device can be accurately measured.

Fig. 3.9. Schematic diagram of Hitachi S-4800 SEM.

3.3.3 Vacuum System Setup

The specific vacuum system, illustrated in *Fig. 3.10*, contains the essential elements typically required to obtain high vacuum. In the designed vacuum system, there are three pumping devices, including two rotary vane vacuum pumps and the turbo molecular pump. Other components of the vacuum system, such as valves and gauges, aid the actions of these pumps. Besides, the charge-couple device (CCD) camera was adopted to capture the glow images. Accordingly, the electrical source was supplied by pulse DC controller. The details functions of the components are described below.

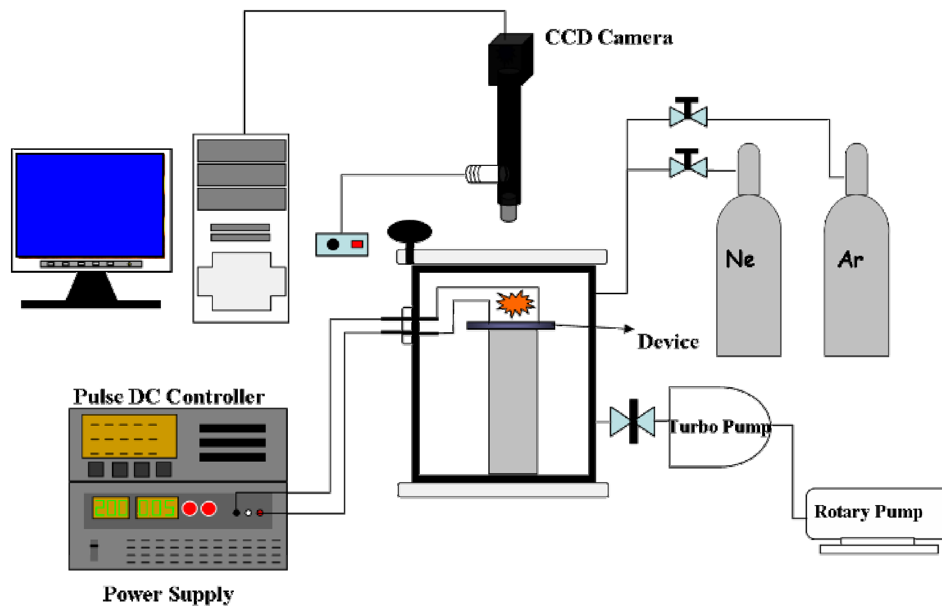

Fig. 3.10. The schematic diagram of the specific vacuum system.

a. Rotary Vane Pump:

The rotary vane pump's hollow body has a rotating cylinder mounted off-axis. In the rotor, two diametrically opposed radially directed vanes are spring-loaded to force contact with the pump body. Since the rotor is positioned off-axis, its motion causes the volume between the vanes and the body to vary during each half turn. The gas inlet port is so positioned that the volume behind the last vane to pass increases, allowing gas to expand into it until the next vane passes. As the volume exposed to the inlet increases, the volume trapped between the vane and the exhaust port decreases. In a single stage pump, the exhaust port has a valve connected to the atmosphere. In a two stage pump, the first stage's exhaust connects directly to the second stage's inlet. Gas exits the pump by bubbling up through the pump's oil reservoir. In either version, the gas is compressed against the final exhaust valve until it exceeds atmospheric pressure, at which point it forces open the exhaust valve and escapes. All the sliding surfaces, the bearings, and gaskets are lubricated and sealed

against gas leaks by the pump's oil. Considering the exhaust pressure illustrates an important but frequently overlooked factor of vane pump operation. With an operating temperature of, typically, 80°C and a gas pressure greater than atmospheric at the exhaust, chemical reaction between the gas and the fluid can increase when pumping corrosive gases and even explode if a hydrocarbon fluid is used when pumping 100% oxygen.

In our designed vacuum system, two rotary vane pumps were used to be fore pumps. First one is a fore pump to vacuum chamber and the other is a fore pump to turbo molecular pump. When the chamber was exhausted below the critical pressure, the turbo molecular pump was turned on to obtain the expectative vacuum degree.

b. Turbo Molecular Pump:

A turbo pump has a stack of rotors resembling a jet engine. Each of rotors which has multiple and angled blades drive at very high speed with tangential direction. Gas molecules, hit by the underside of the angled blades, move with momentum in the direction of the higher pressure exhaust. Turbo pumps come in two basic designs. In the SNECMA design (named after a French jet-engine manufacturer) all gas enters through the main flange at the visible single-end of the pump; the Pfeiffer (named after the original turbo pump's manufacturer) double-ended design, has two rotors set-mounted on a common axle. Gas enters the pump through a right angle port between the two rotor sets and exits into an exhaust manifold connecting the two ends of the pump. For normal commercially available pumps, pumping speeds range from approximately 20 L/s to 3,000 L/s (although some turbo pumps manufactured in Russia are quoted with pumping speeds of 20,000 L/s). All gases are pumped at roughly the same rate. One pump, for example, listed with 450 L/s for nitrogen, has a pumping speed for hydrogen of 310 L/s. Turbo pumps reach full operating speed

within a few minutes of switch-on, making a separate roughing line unnecessary since the accelerating turbo can rough the chamber. The trick is to match chamber volume and the effective pumping speed, and to time the turbo pump's start so its rotational speed is high enough to prevent backstreaming when the chamber reaches 10^{-1} Torr (that is, when an oil-sealed mechanical pump's relative backstreaming rate starts its rapid rise). With proper venting, a turbo pump can be entirely halted in under one minute. This slight delay before the chamber reaches atmospheric pressure and can be opened usually works for most applications. The benefit is clear. If the pump does not run while venting the chamber, we have no need for a high vacuum valve between pump and chamber. Further, in a correctly designed and operated system, the turbo pump does not allow oil vapor to backstream so that the system does not require an LN_2 trap between chamber and pump. A turbo pump's high rotational speeds (some small diameter units operate at 60,000 rpm) put serious strain on the shaft bearings. Most manufacturers now offer light-weight ceramic ball bearings with grease lubrication since this combination is both light, lowering the momentum of the bearing, and has a low bearing-lubricant vapor pressure at the pump's working temperature. More recently, manufacturers have begun offering magnetically levitated bearings which are either permanent magnets for the small sized pumps or a combination of permanent and dynamic magnetic fields, supporting the shaft without contact. Magnetically levitated pumps (such as those manufactured by Shimadzu) include non-contact bearings, resulting in a turbo pump that has true zero oil-vapor backstreaming with bearings that never wear down.

Using turbo molecular pump to obtain the expectative vacuum degree can avoid the oil contamination. The exhaust was connected to the second rotary vane pump, which produces a pressure low enough for the turbo molecular pump to work efficiently. In general, the turbo molecular pump can be a very versatile pump. It can

generate many degrees of vacuum from intermediate vacuum (~10^{-4} Torr) up to ultra-high vacuum levels (~10^{-10} Torr).

c. Gauge:

In order to check the vacuum degree of the chamber, two kinds of gauges were used to measure the different range of the vacuum degree.. The Baratron gauge is general purpose pressure transducers designed to provide accurate and repeatable pressure measurement in the range from 1 K Torr to as low as 0.05 Torr Full Scale (FS). However, the higher vacuum degree can be detected by ionization gauge which is used to measure the residual pressure of vacuum in the high vacuum and ultra-high vacuum ranges. Most of the ionization gauge cannot measure the higher pressures of the medium vacuum range, where the Pirani gauges, thermocouple gauges and convention gauges are use instead.

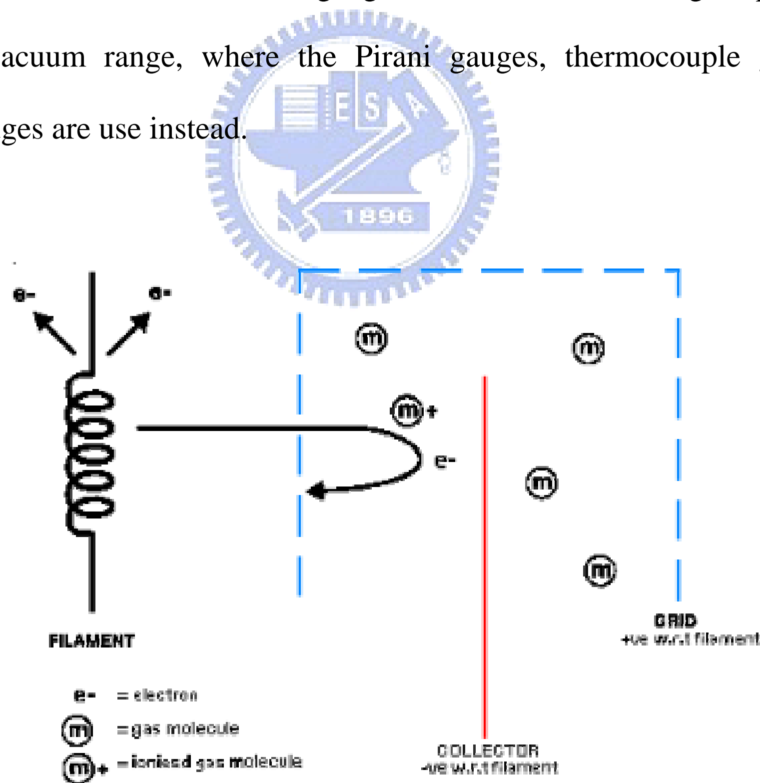

Fig. 3.11. The schematic of ionization gauge.

The ionization gauge consists of three distinct parts, shown in *Fig. 3.11*, including the filament, the grid and the collector. The filament is used for the

production of electrons by thermal emission. A $+v_e$ charge on the grid attracts the electrons away from the filament; they circulate around the grid passing through the fine structure many times until eventually they collide with the grid. Gas molecules inside the grid may collide with circulating electrons. The collision can result in the gas molecule being ionized. The collector inside the grid is $-v_e$ charged and attracts these $+v_e$ charged ions. Likewise they are repelled away from the $+v_e$ grid at the same time. The number of ions collected by the collector is directly proportional to the number of molecules inside the vacuum system. By this method, measuring the collected ion current gives a direct reading of the pressure. The above paragraph is a simplification of what happens. The design of the gauge head effects how efficiently electrons are produced, how long they survive, and how likely they are to collide with a molecule. Combining these factors together gives the gauge a sensitivity. As a general rule, the higher the sensitivity, the more efficient the operation of the gauge.

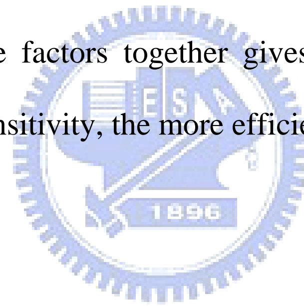

d. Pulse DC Controller:

The fabricated device was excited by pulse DC controller, including a DC-pulse power controller (SPIK 2000A, SHENCHANG ELECTRIC CO., LTD) and a direct current (DC) power supply. The power supply provides the voltage to DC-pulse power controller and forms the output of bipolar voltage waveform. The bipolar voltage waveform, having the duty ratio with 20%, was applied with different frequencies between the interdigitated Chromium (Cr) electrodes which has a 20 μm gap by the pulse DC controller. *Fig. 3.12* shows the photograph of the pulse DC controller set using in this thesis.

Fig. 3.12. Photograph of pulse DC controller and DC power supply.

e. Charge-Couple Device Camera:

The images of the glow dicharge from the micro-plasma device were captured by using a color charge-coupled device (CCD) camera (Watec, WAT-202D) with zoom lenes. The signal of the color charge-coupled device (CCD) cam era captured was connected to a personal computer by a capture card (UPMOST, MTV Video Capture).

Chapter 4

Experimental Results and Discussion

4.1 Introduction

The characterizations of the interdigitated electrode micro-plasma device will be presented in this chapter. The structure of interdigitated electrode micro-plasma device was fabricated agreement with the designed structure by photolithographic techniques. The interdigitated electrode micro-plasma device which has a simple fabrication process offers the advantages, such as low ignition voltage, low cost and stable glow discharge. In the following sections, the electrical properties on neon discharge have been examined by bipolar voltage waveform with different frequencies of 10 kHz, 14.3 kHz and 25 kHz. The relationship between the ignition voltage and dielectric layer thickness is also investigated. In addition, the electrical properties on neon discharge have been examined by bipolar voltage waveform with different argon gas concentration.

4.2 The Features of the Interdigitated Electrode Micro-Plasma Device

The thick photoresist (XP SU-8 3050) is design specifically for ultra-thick, high-aspect-ratio microelectrical mechanical systems (MEMs). In addition, the decomposition temperature which is about 380 °C for SU-8 can resist the plasma. Therefore, the thick photoresist can be served as a barrier rib to take the place of the photo-definable glass. Since the thick photoresit was spin-coated on the substrate, the

incompact issue of the photo-definable glass can be solved. Besides, the geometric pattern was obtained accurately with the interdigitated electrode by aligner mask. The photo-definable glass was attached with the screen electrodes in order to realize the proposed device easily.

The structure of the interdigitated electrode micro-plasma device was measured by the scanning electron microscope (Hitachi S-4800). The electrode thickness, dielectric thickness, barrier rib height, aperture size of geometric pattern and cross-section of fabricated device can be accurately measured. *Fig. 4.1* shows the cross-section of the square-shape interdigitated electrode micro-plasma device. The barrier rib has an aspect ratio (height over width) of 3 where height (60 μm) is high enough to avoid the cross-talk.

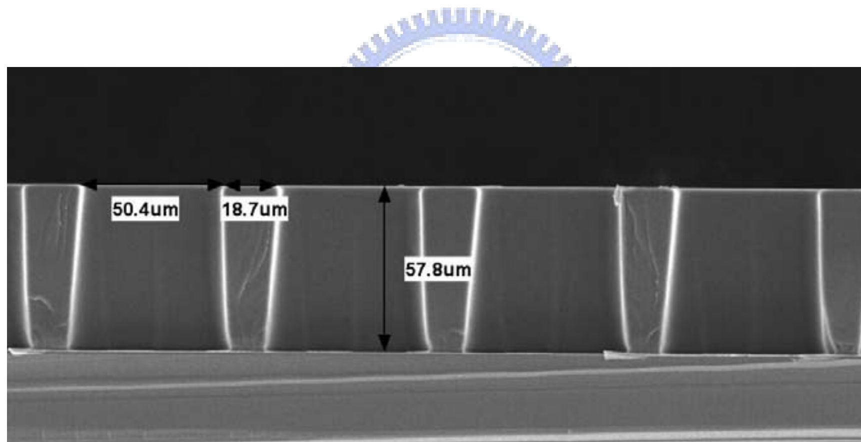

(a) Cross-section

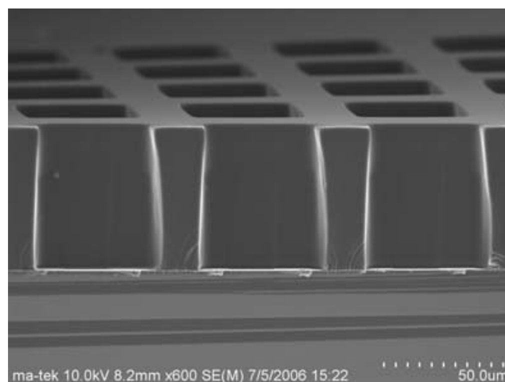

(b) Cross-section with a tilt angle

Fig. 4.1. The SEM image of the square-shape interdigitated electrode micro-plasma device.

Several geometric patterns are also developed by the designed mask. By the lithographic techniques, the geometric pattern can obtain at the right position, including two electrodes. It need not make screen electrodes and the larger array can be realized efficiently. The features of the interdigitated electrode micro-plasma device, shown in *Fig. 4.2*, were measured and different patterned shapes are also illustrated in *Fig. 4.3*.

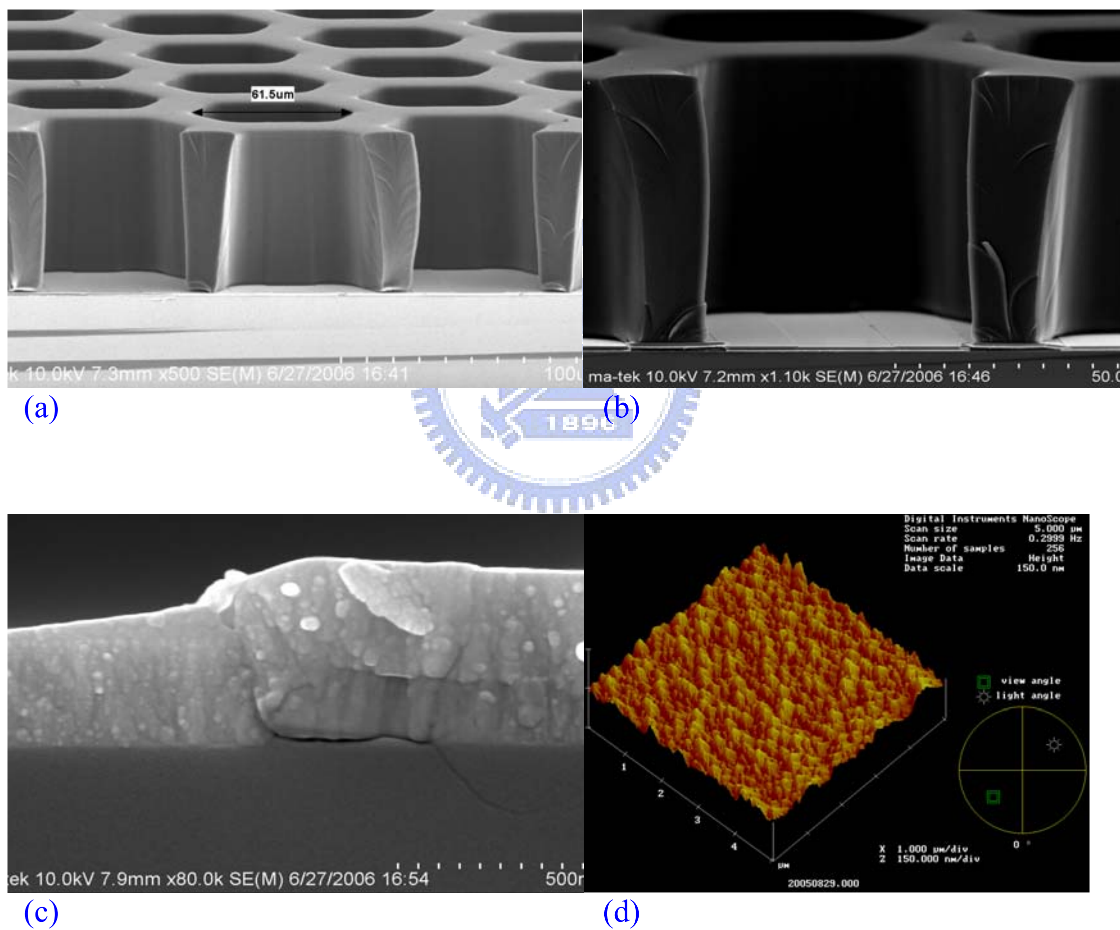

Fig. 4.2. The features of the hexagon-shaped interdigitated electrode micro-plasma device. (a) cross-section with a tilt angle (b) two electrodes confined to the patterned shape (c) cross-section of the dielectric layer and electrode (d) surface morphology of HfO_2.

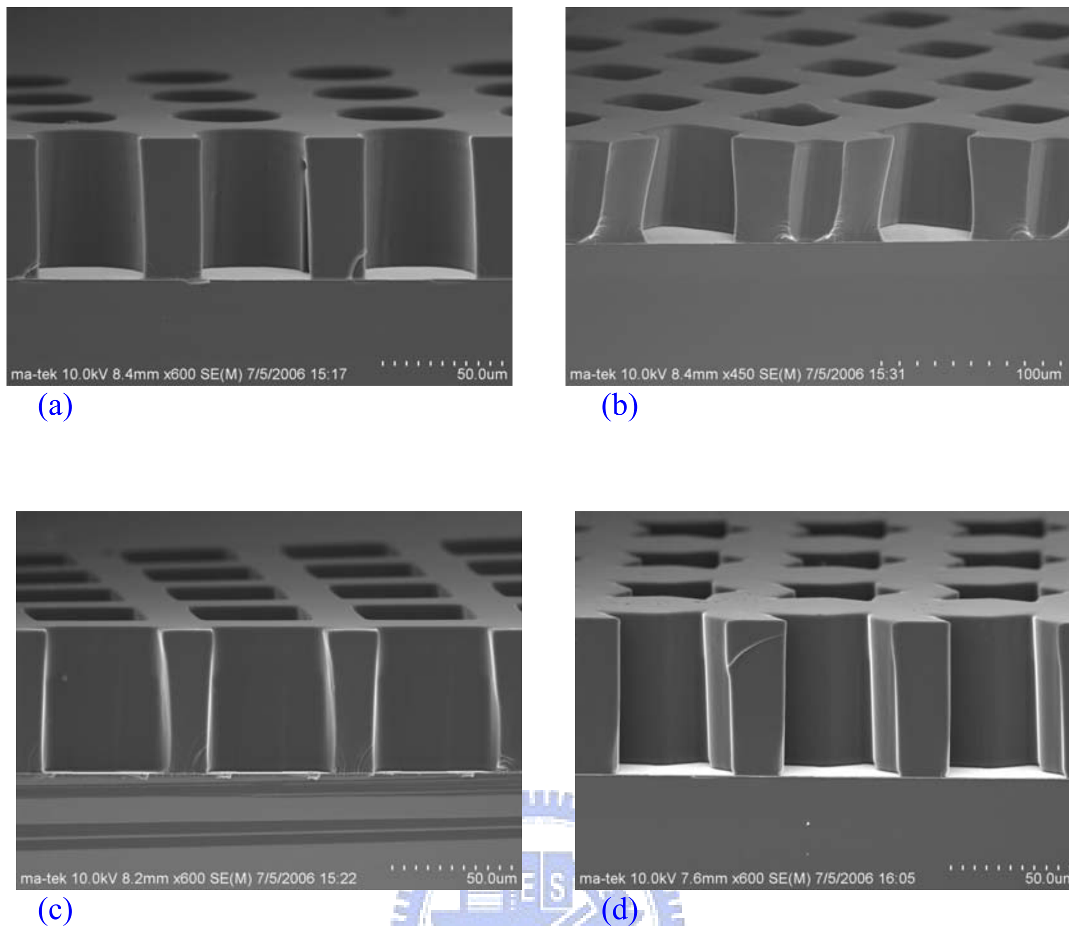

Fig. 4.3. The different patterns of the interdigitated electrode micro-plasma device. (a) circle-shaped (b) diamond-shaped (c) square-shaped and (d) star-shaped.

4.3 The Electrical Properties in Neon Gas

The photograph of the fabricated device, shown in *Fig. 4.4*, was investigated in a vacuum chamber. Before measuring the fabricated device, the electrode pads should be connected with electric wires by sliver paste. The torr seal was used to cover the electric wires with the sliver paste.

The electrical properties of the device are investigated in the specially designed vacuum system. The vacuum chamber was pumped down to $2x10^{-6}$ Torr by a turbo molecular pump and back-filled with the research vacuum grade of neon gas between

300 and 800 Torr. The bipolar voltage waveform with different frequencies is applied between the Cr electrodes.

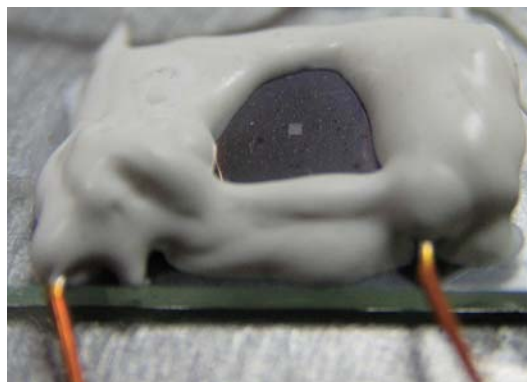

Fig. 4.4. The photograph of the fabricated device with the electric wire.

4.3.1 Relationship between voltage and pressure with different bipolar voltage waveform frequency

The voltage margin, the ignition voltage (V_f) and the minimum sustain voltage (V_s), for hexagon-shaped interdigitated electrode micro-plasma device operating in neon gas at pressure between 300 and 800 Torr is presented in *Fig. 4.5*. The interdigitated electrode micro-plasma device is driven by a bipolar voltage waveform which has the frequencies of 10, 14.3 and 25 kHz. It should be noted that the ignition voltage reduces by increasing the operating pressure. The higher operating pressure causes the decreased mean free path of the neon gas (greater densities of gas molecules). The mean free path is the average distance traveled by a gas atom between collisions with another. In addition, the probability of collision is related to the collision frequency which is the number of gas atom collisions per unit time. It means that increasing the pressure causes a higher probability of collision. Therefore, the ignition voltage is reduced by increasing the operating pressure.

(a)

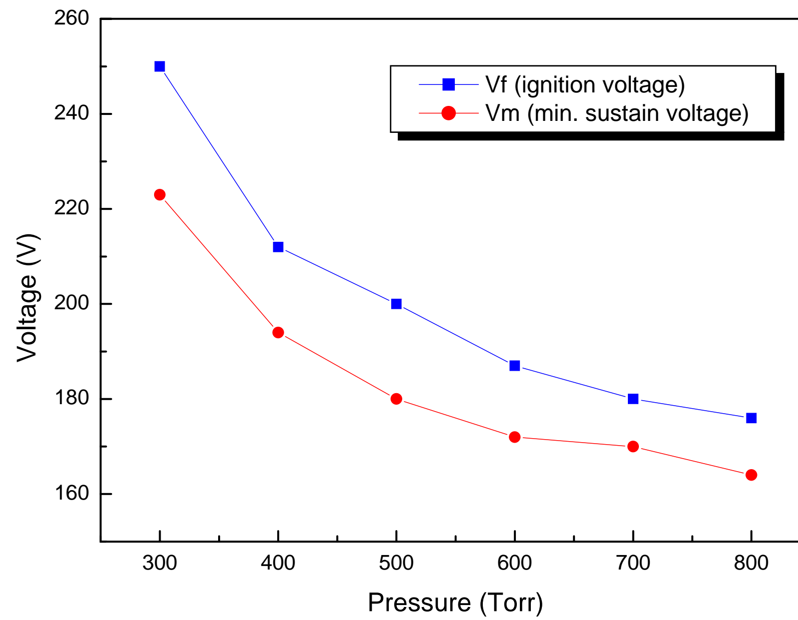

(b)

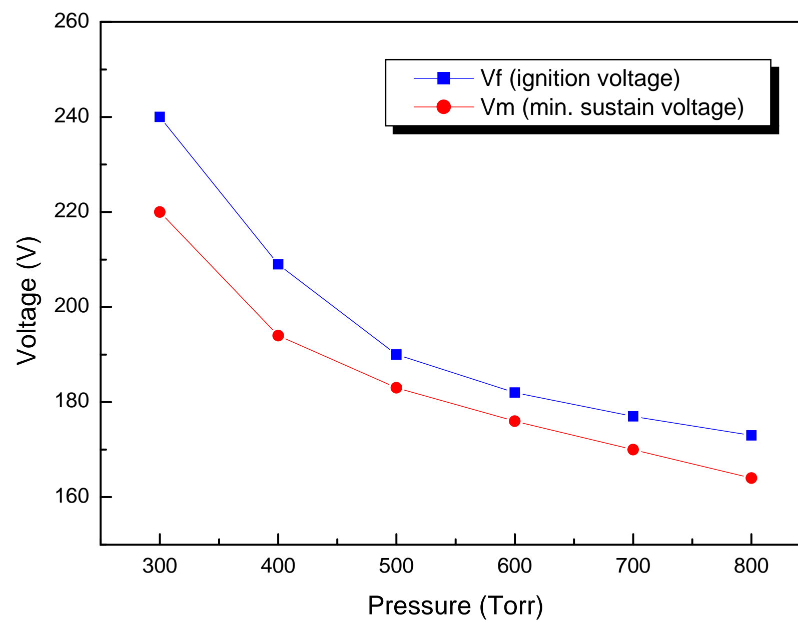

(c)

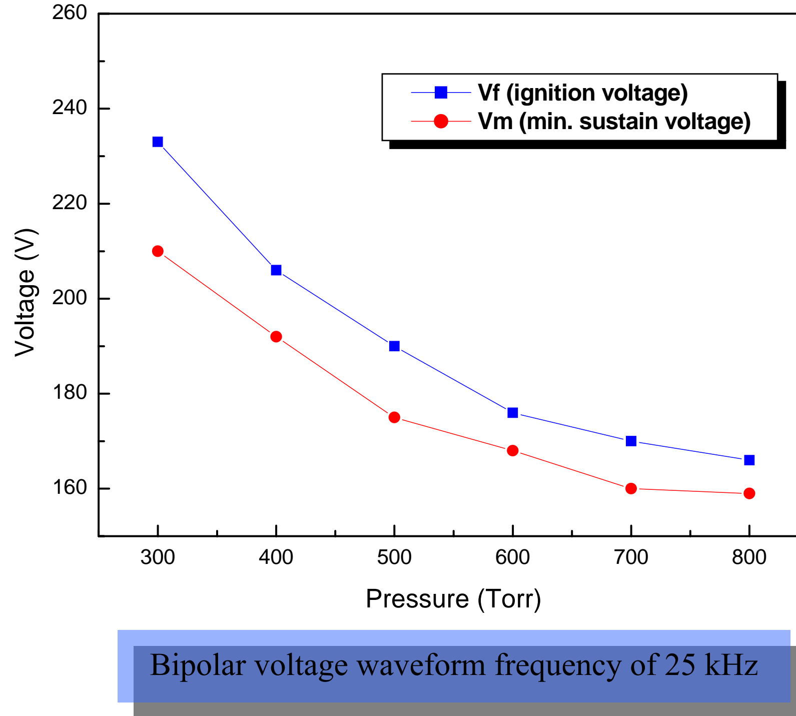

Fig. 4.5. The margin of the firing voltage and the minimum sustain voltage for the interdigitated electrode micro-plasma device with different bipolar voltage waveform frequency of (a) 10, (b) 14.3 and (c) 25 kHz in neon gas at pressure from 300 to 800 Torr.

Accordingly, with increasing the frequency of bipolar voltage waveform, the ignition voltage is getting lower at the same pressure. It is due to the impedance related to the frequency.

$$Z_C = \frac{1}{j\omega C} \quad (1)$$

where ω, angular frequency, is equal to $2\pi f$. From Eq. (1), higher frequency causes the impedance to decrease; however, the ignition voltage reduces by increasing the frequency of the bipolar voltage waveform, shown in *Fig. 4.6*.

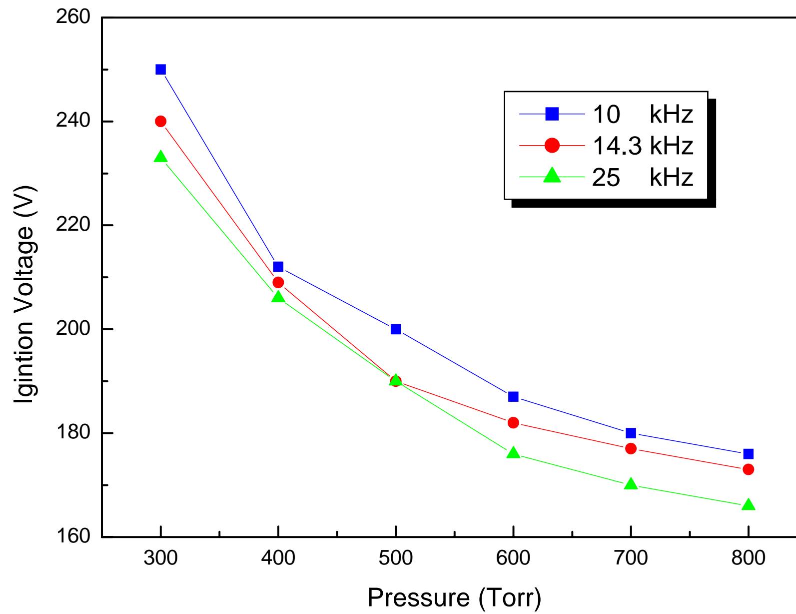

Fig. 4.6. The ignition voltage for the interdigitated electrode micro-plasma device with different bipolar voltage waveform frequencies in neon gas at pressure 300 to 800 Torr.

4.3.2 Relationship between ignition voltage and pressure with different dielectric layer thickness

The characteristics of ignition voltage and pressure in neo gas with different dielectric layer thickness are shown in *Fig. 4.7*. The ignition voltage also decreases with reducing dielectric layer thickness, meaning the dielectric layer capacitance increases. This is due to the division of the externally applied voltage over the gas gap and dielectric layer. The applied sustaining voltage V_s is deduced from voltage across the gas gap V_g and the voltage across the dielectric layer V_d by

$$V_s = V_g + V_d \quad (2)$$

with

$$V_d = V_d(0) + \frac{S}{C}\int_0^t J_T dt \quad (3)$$

where J_T is the instantaneous total current density and C the equivalent capacitance of the dielectric layer, and S the discharge surface [33][34]. Here, we assume the gas gap has the same condition, meaning the V_g is considered as constant. According to the capacitance formula, $C = \frac{\varepsilon A}{d}$, reducing the dielectric layer thickness causes the capacitance to increase. The voltage across the dielectric layer, V_d, reduces relatively at the same dielectric layer. The equivalent circuit model to estimate the capacitance of the micro-plasma device is shown in *Fig. 4.8*.

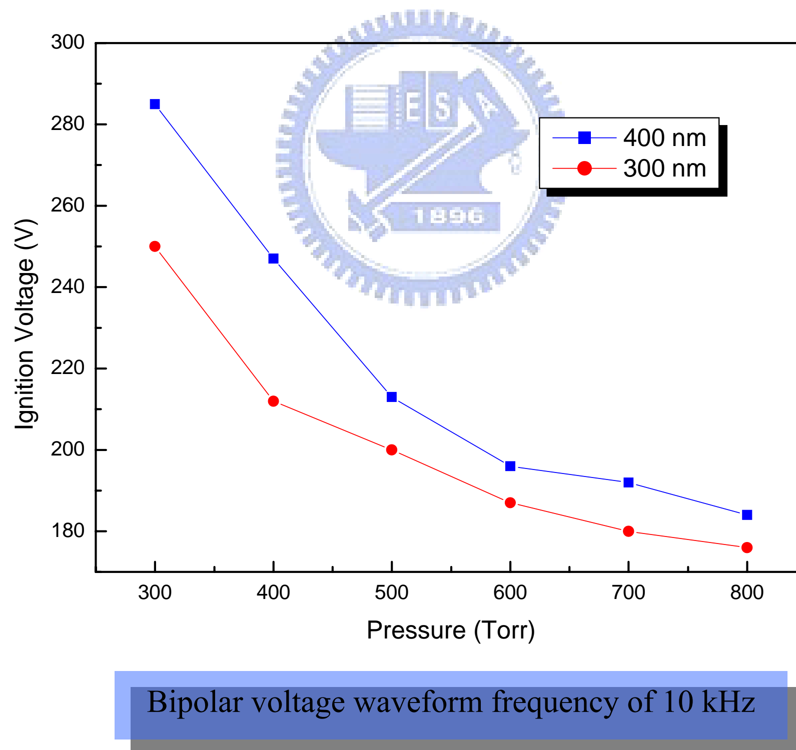

Fig. 4.7. The firing voltage for the interdigitated electrode micro-plasma device with different dielectric layer thickness in neon gas at pressure from 300 to 800 Torr.

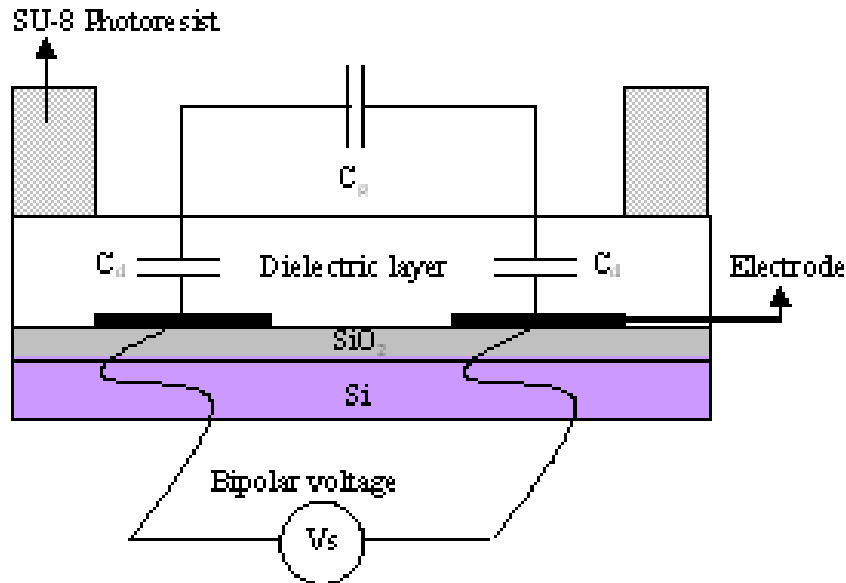

Fig. 4.8. The equivalent circuit model to estimate the capacitance of the interdigitated electrode micro-plasma device.

4.4 The Electrical Properties in Neon-Argon Gas Mixtures

The ignition voltage of the diamond-shaped interdigitated electrode micro-plasma device is also investigated in pure neon gas at pressure from 300 to 800 Torr. The ignition voltage, where the fabricated device has 300 nm dielectric layer thickness, reduces as a function of neon pressure. In addition, the characteristic of the pure argon gas is also measured at the same pressure range. *Fig. 4.9* shows the comparison of ignition voltage with pure neon and pure argon gas. The ignition voltage of pure argon gas reaches a lower minimum value and becomes larger after 500 Torr. The main reason for the fact that the relationship of ignition voltage versus gas pressure becomes a curve is due to the *Paschen's Law*. The law essentially states that, at higher pressures (above a few Torr) the breakdown characteristics of a gap are a function (generally not linear) of the product of the gas pressure and the gap length,

usually written as V= f(*pd*), where *p* is the pressure and *d* is the gap distance. The reduction of the dimensions of micro-plasma device afforded by MEMS can be operated at atmospheric pressure. However, the ignition voltage of neon reduces by increasing the operating pressure because the values of *pd* are small enough. In addition, after the minimum value of the critical *pd*, the ignition voltage of the argon gas increases.

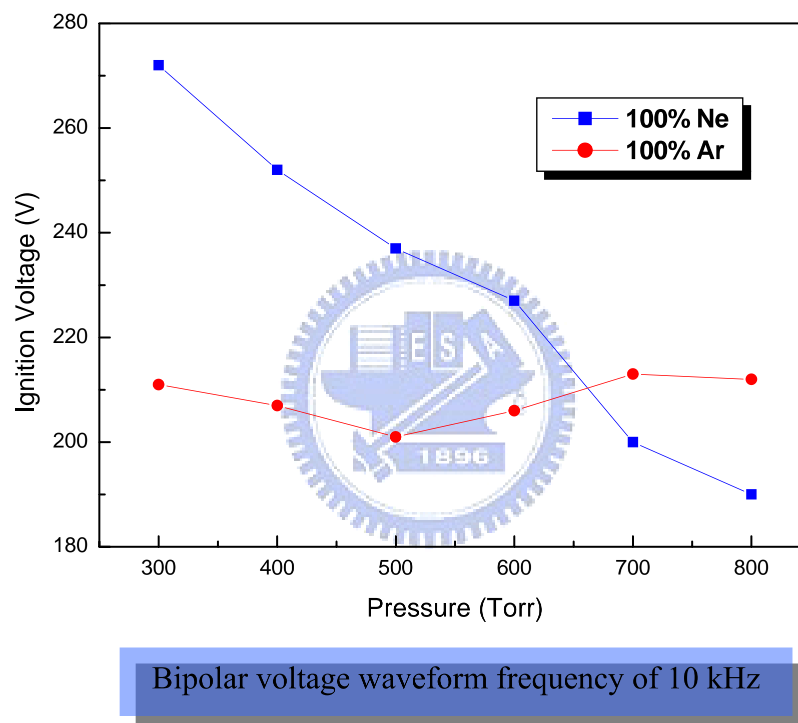

Fig. 4.9. The ignition voltage for the interdigitated electrode micro-plasma device in pure neon and argon gas at pressure from 300 to 800 Torr.

The mixtures, containing 1% and 5% of the argon gas, all behave in a similar manner to the pure neon gas. The ignition voltage of the neon-argon mixtures, shown in *Fig.4.10*, has a lower value than the pure neon gas under similar conditions. Also, the voltage margin decreases by the increase of argon gas concentration.

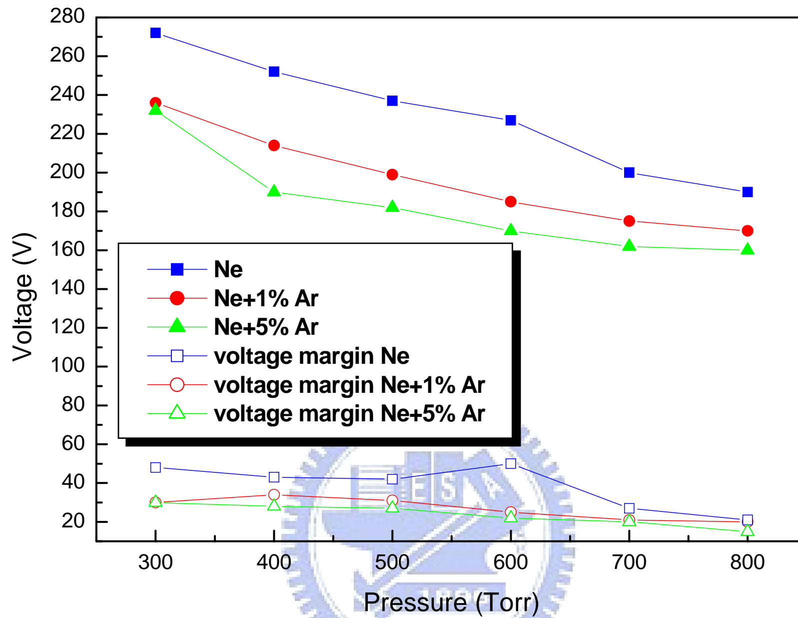

Fig. 4.10. The characteristics of firing voltage and different concentrations of argon gas for the interdigitated micro-plasma device with bipolar voltage waveform frequency of 10 kHz at pressure from 300 to 800 Torr.

However, the mixtures are used to provide an improvement in efficiency of ionization due to the Penning effect and a reduction in dissociative recombination losses. It could have an advantage over single pure neon gas in two ways. Firstly, the energy required to produce a give number of ions should be reduced since energy consumed in the production of metastable states is still available for ionization. Secondly, the probability of ion loss by dissociative recombination is lower, since the partial pressure of minority gas is so low that the probability of molecular ion formation, required for dissociative recombination, is very small.

The metastable state of neon is larger than the ionization potential of argon. Besides, the lifetime of a neon atom in this state is long enough to make many thousands of collisions at moderate argon gas concentrations. When the excited neon atoms collide with argon atoms, the energy exchange takes place and the ionization of argon atoms occur. A relatively small amount of argon in the neon will ensure that the excited neon atoms will collide with an argon atom in a very high probability. In such a collision, the excited state of the neon atom will return to the ground state and loss its energy to ionize the argon atom.

4.5 The Glow Images of the Interdigitated Electrode Micro-Plasma Device

The glow of the 5x5 hexagon-shaped arrays, shown in *Fig. 4.11*, is uniform and operating in 300 Torr of neon gas. The driving voltage and frequency are 250 V and 10kHz, respectively. After operating the micro-plasma device, however, the barrier rib is still well-found.

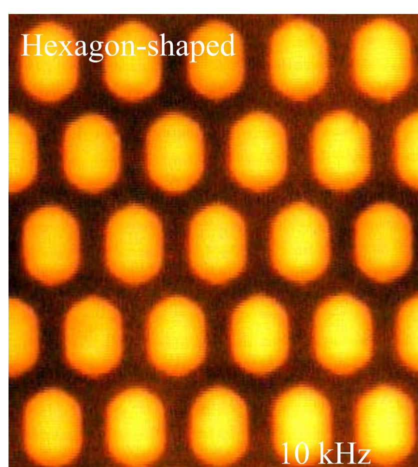

Fig. 4.11. Photograph of the 5x5 arrays of the interdigitated micro-plasma device with a hexagonal structure operating in 300 Torr of neon gas.

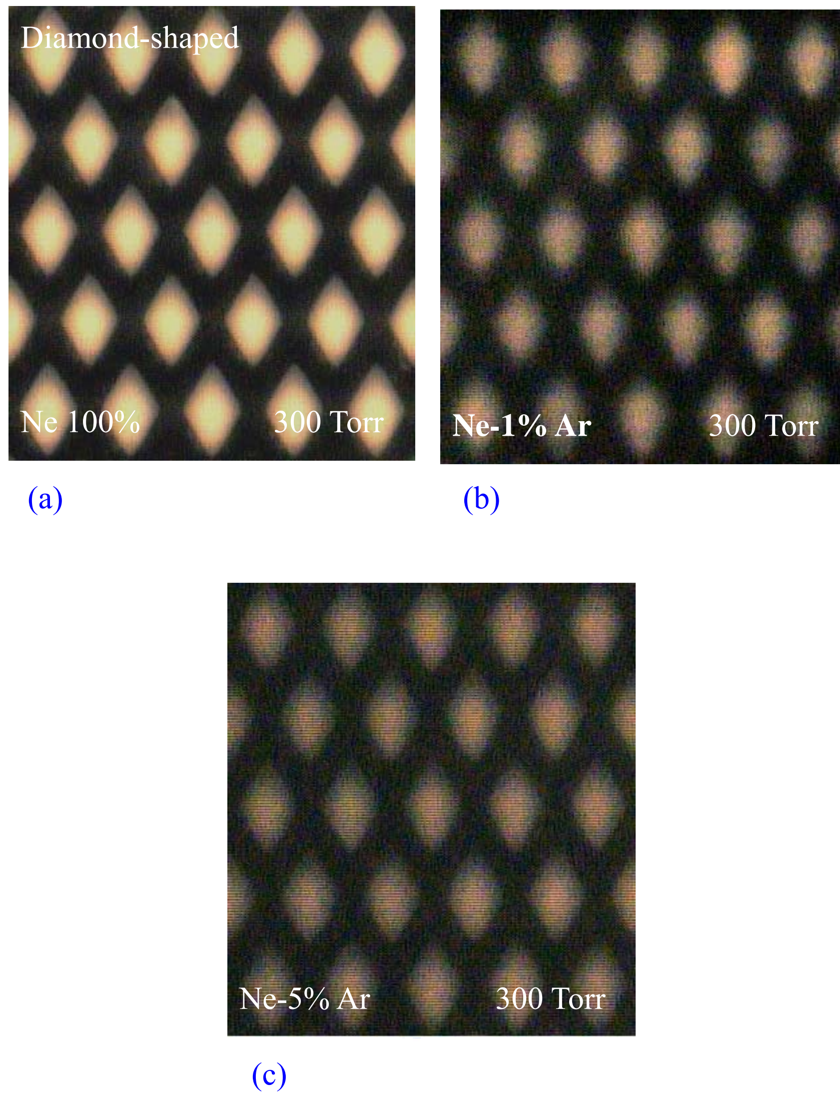

(a) (b)

(c)

Fig. 4.12. Photograph of the 5x5 arrays of the micro-plasma device with a diamond structure operating in 300 Torr of (a) neon gas, (b)neon(99%)-argon(1%), and (c) neon(99%)-argon(5%) mixtures.

In addition, the glow of the 5x5 diamond-shaped arrays, shown in *Fig. 4.12(a)*, is uniform and operating in 300 Torr of neon gas. The driving voltage and frequency are 272 V and 10kHz, respectively. The glow images in neon-1% argon and neon-5% argon gas mixtures are also shown in *Fig. 4.12(b)* and *Fig. 4.12(c)*. The glow images

show the differences between the pure neon gas and the neon-argon gas mixtures. The arrays in neon-argon gas mixtures have a little purple visible light. The diamond-shaped micro-plasma device provides uniform plasma and solves the issue which is the misfiring plasma between barrier rib and substrate. Even though the real plasma provides clear and bright plasma, the CCD camera did not express the quality because of poor resolution.

Chapter 5

Conclusions

There exists a gap in between because of the incompactness of photo-definable glass and substrate. This issue will influence individual cells discharging. The thick photoresist (XP SU-8 3050) served as a barrier rib instead of the photo-definable glass was feasible. Since the thick photoresit (XP SU-8 3050) can be spin coated on the substrate to slove the incompact issue of the photo-definable glass. In addition, the barrier rib which has height of 60 μm is high enough to avoid the cross-talk. After operating the micro-plasma device, however, the barrier rib is still well-found. Any geometric or high resolution pattern is feasible and suitable for many valuable applications.

The interdigitated electrode micro-plasma device with hexagonal structure consisting of 5x5 arrays has been operated and reported in this thesis. Accordingly, the interdigitated electrode micro-plasma device utilizing thick photoresist as a barrier rib exhibits uniform glow discharge and has low ignition voltage with bipolar voltage waveform. The ignition voltage of the interdigitated electrode micro-plasma device was reduced as a function of neon pressure. There are two parameters have been investigated:

(1) Thinner dielectric Layer thickness has lower ignition voltage of plasma.
(2) Higher bipolar voltage waveform frequency has lower ignition voltage of plasma.

Furthermore, the interdigitated electrode micro-plasma device with diamond structure consisting of 5x5 arrays has been also operated and reported in this thesis. The neon-argon gas mixtures used to as fillings in the experimental chamber have the advantage over pure neon gas. Because of the Penning effect, the ignition voltage of the interdigitated electrode micro-plasma device was reduced as a function of argon concentrations. In other hand, higher argon concentration has lower ignition voltage for the interdigitated electrode micro-plasma device. There could, however, be an economic advantage in the use of mixtures.

Reference

[1] A. D. White, J. Appl. Phys. **30**, 711 (1959).

[2] R. L. Johnson, D. L. Bitzer and H. G. Slottow, IEEE Trans. Electron Devices, **ED-18**, 642 (1971).

[3] K. H. Schoenbach, R. Verhappen, T. Tessnow, F. E. Peterkin, and W. W. Byszewski, Appl. Phys. Lett., **68**, 13 (1996).

[4] J. W. Frame, P. C. John, T. A. DeTemple, and J. G. Eden, Appl. Phys. Lett., **71**, 1165 (1997).

[5] K. H. Schoenbach, A. El-Habachi, W. Shi, and M. Ciocca, Plasma Sources Sci. Technol. **6**, 468 (1997).

[6] G. J. Pietsch and V. I. Gibalov, Pure & Appl. Chem., **70**, 1169 (1998).

[7] K. C. Choi, IEEE Trans. Electron Devices, **46**, 2256 (1999)

[8] S. J. Park, C. J. Wagner, C. M. Herring and J. G. Eden, Appl. Phys. Lett., 77, 199 (2000).

[9] M. Moselhy, W. Shi, R. H. Stark and K.H. Schoenbach, IEEE Trans. Plasma Sci., **30**, **198** (2002).

[10] S. J. Park and J. G. Eden, Appl. Phys. Lett., **81**, 4529 (2002).

[11] K. S. Szalowski, J. Sentek, K. Krawczyk and K. Radomyska, Polish J. Chem., 77, 1351 (2003).

[12] D. Mariotti, P. Maguire, C. M O Mahony and J. McLaughlin, Plasma Sources Sci. Technol., **13**, 576 (2004).

[13] Paschen F 1916 *Ann. Phys.* **50** 901

[14] G¨untherschulze A 1923 *Z. Tech. Phys.* **19** 49

[15] Walsh A 1956 *Spectrochim. Acta* **7** 108

[16] L. D. Biborosch, Appl. Phys. Lett., **75**, 3926 (1999).

[17] J. Chen, S. J. Park, J. G. Eden and C. Liu, The 11th International Conference on Solid-State Sensors and Actuators (2001).

[18] S. J. Park, J. Chen, C. J. Wagner, N. P. Ostrom, C. Liu and J. G. Eden, IEEE J. Sel. Top. Quantum Electron., **8**, 387 (2002).

[19] J. G. Eden, S. J. Park, N. P. Ostrom, S. T. McCain, C. J. Wagner, B. A. Vojak1, J. Chen, C. Liu, P von Allmen, F. Zenhausern, D. J. Sadler, C. Jensen, D. L. Wilcox and J. J. Ewing, J. Phys. D: Appl. Phys. **36**, 2869 (2003).

[20] S. J. Park and J. G. Eden, Plasma Phys. Control. Fusion, **47**, B83 (2005).

[21] S. J. Park, K. F. Chen, N. P. Ostrom and J. G. Eden, Appl. Phys. Lett., **86**, 111501 (2005).

[22] K. F. Chen, N. P. Ostrom, S. J. Park and J. G. Eden, Appl. Phys. Lett., **88**, 061121 (2005).

[23] S. J. Park, K. S. Kim and J. G. Eden, Appl. Phys. Lett., **99**, 026107 (2005).

[24] K. H. Becker, K. H. Schoenbach and J. G. Eden, J. Phys. D: Appl. Phys., **39**, R55 (2006).

[25] K. Becker, A. Koutsospyros, S. M. Yin, C. Christodoulatos, N. Abramzon, J. C. Joaquin and G. Brelles-Marino, Plasma Phys. Control. Fusion, **47,** B513 (2005).

[26] J. H. Brownell, A. G. Nerukh, N. K. Sakhnenko, S. V. Zhilkov and A. A. Aleksandrova, J. Phys. D: Appl. Phys., **38,** 1658 (2005).

[27] P. von Allmen, D. J. Sadler, C. Jensen, N. P. Ostrom, S. T. McCain, B. A. Vojak, and J. G. Eden, Appl. Phys. Lett., **82**, 4447 (2003).

[28] J. G. Eden, C. J. Wagner, J. Gao, N. P. Ostrom and S. J. Park, Appl. Phys. Lett., 79, 4304 (2001).

[29] S.-O. Kim, J. Gary Eden, IDMC'05, 84 (2005).

[30] S.-O. Kim, J. Gary Eden, SID'05 Digest of Tech Papers, 1029 (2005).

[31] F. Chen, *Introduction to Plasma Physics and Controlled Fusion*, Plenum Press, New York, New York, 1984.

[32] M. A. Liebermann and A. J. Lichtenberg, *Principles of Plasma Discharges and Materials Processing*, John Wiley & Sons, Inc., New York, New York, 1994.

[33] G. Oversluizen, T. Dekker, M. F. Gillies, and S. T. de Zwart, SID'03, Digest of Tech Papers, 28 (2003).

[34] J. Meunier, Ph. Belenguer, and J. P. Boeuf, J. Appl. Phys., **78**, No.2, 731 (1995).